High-resolution thermal imaging in the Antarctic marginal ice zone: Skin temperature heterogeneity and effects on heat fluxes

Ippolita Tersigni[1], Alberto Alberello[2], Gabriele Messori[3], Marcello Vichi[4], Miguel Onorato[5], and Alessandro Toffoli[1]

[1]The University of Melbourne
[2]University of East Anglia
[3]Uppsala University
[4]University of Cape Town
[5]Universita' di Torino

May 25, 2023

Abstract

Insufficient in-situ observations from the Antarctic marginal ice zone limit our understanding and description of relevant mechanical and thermodynamic processes that regulate the seasonal sea ice cycle. Here we present high-resolution thermal images of the ocean surface and complementary measurements of atmospheric variables that were acquired underway during one austral winter and one austral spring expedition in the Atlantic and Indian sectors of the Southern Ocean. Skin temperature data and ice cover images were used to estimate the partitioning of the heterogeneous surface and calculate the heat fluxes to compare with ERA5 reanalyses. The winter marginal ice zone was composed of different but relatively regularly distributed sea ice types with sharp thermal gradients. The surface-weighted skin temperature compared well with the reanalyses due to a compensation of errors between the sea ice fraction and the ice floe temperature. These uncertainties determine the dominant source of inaccuracy for heat fluxes as computed from observed variables. In spring, the sea ice type distribution was more irregular, with alternation of sea ice cover and large open water fractions even 400 km from the ice edge. The skin temperature distribution was more homogeneous and did not produce substantial uncertainties in heat fluxes. The discrepancies relative to reanalysis data are however larger than in winter and are attributed to biases in the atmospheric variables, with the downward solar radiation being the most critical.

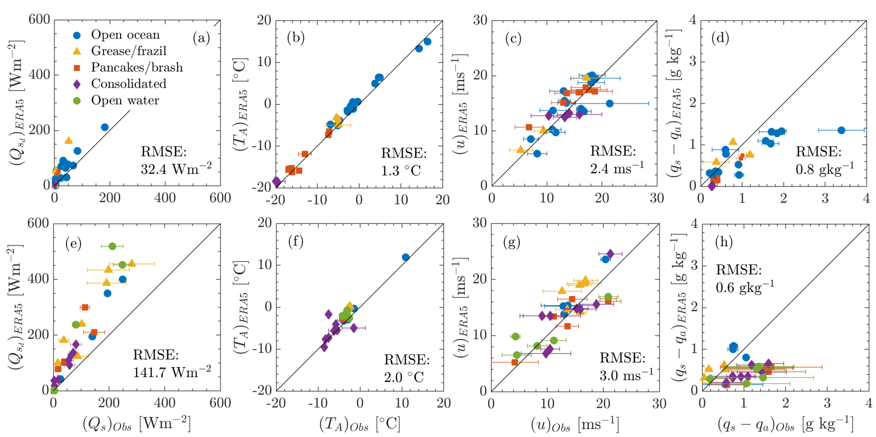

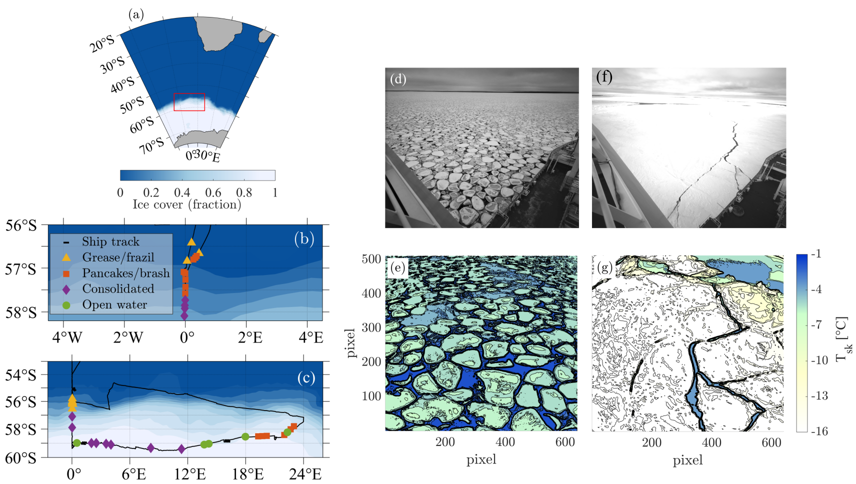
(a)
20°S
30°S
40°S
50°S
60°S
70°S
0°
30°E
Ice cover (fraction)
0 0.2 0.4 0.6 0.8 1
(b)
Ship track
Grease/frazil
Pancakes/brash
Consolidated
Open water
56°S
57°S
58°S
4°W 2°W 0° 2°E 4°E
(c)
54°S 56°S 58°S 60°S
0° 6°E 12°E 18°E 24°E
(d)
(f)
(e)
(g)
pixel
T_{sk} [°C]
-1 -4 -7 -10 -13 -16

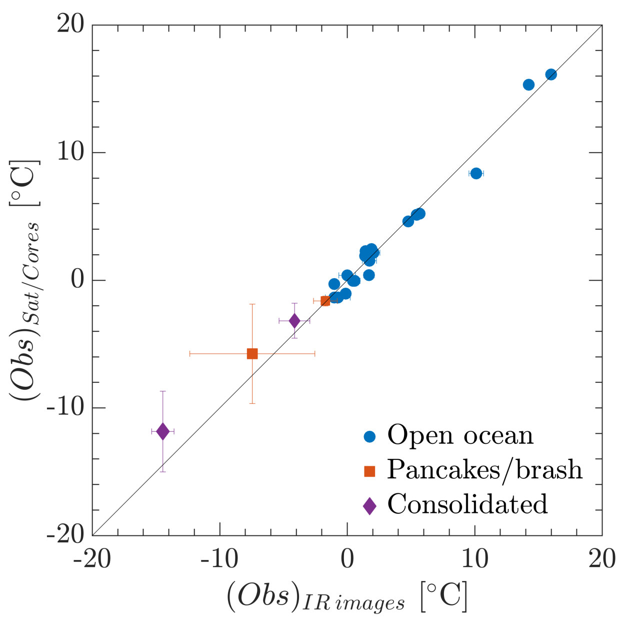
$(Obs)_{Sat/Cores}$ [°C]
$(Obs)_{IR\,images}$ [°C]
Open ocean
Pancakes/brash
Consolidated
20 10 0 -10 -20

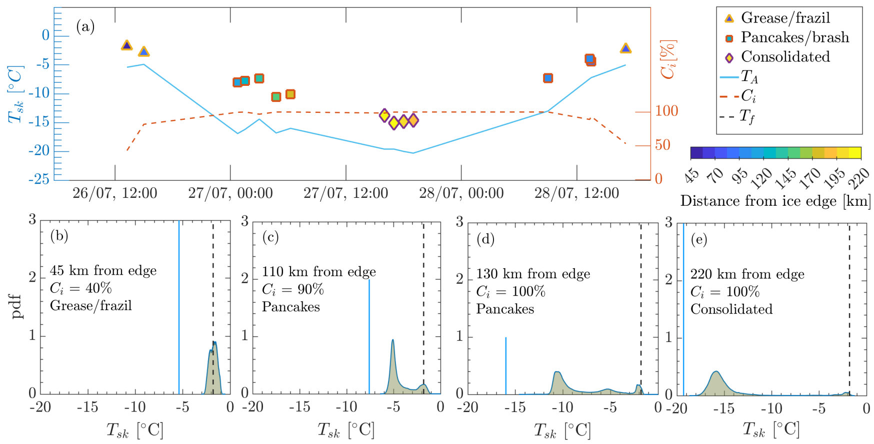
(a)
Grease/frazil
Pancakes/brash
Consolidated
T_A
C_i
T_f
Distance from ice edge [km]
26/07, 12:00
27/07, 00:00
27/07, 12:00
28/07, 00:00
28/07, 12:00
(b)
45 km from edge
C_i = 40%
Grease/frazil
(c)
110 km from edge
C_i = 90%
Pancakes
(d)
130 km from edge
C_i = 100%
Pancakes
(e)
220 km from edge
C_i = 100%
Consolidated
pdf
T_{sk} [°C]

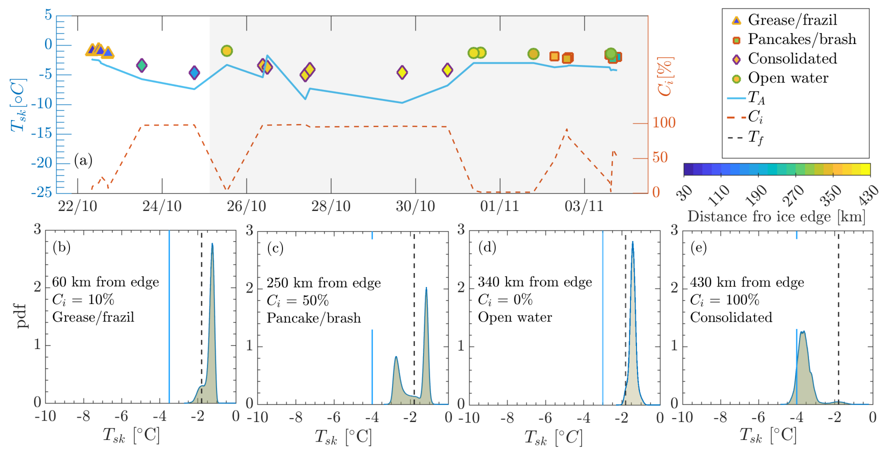
(a)
Grease/frazil
Pancakes/brash
Consolidated
Open water
T_A
C_i
T_f
Distance fro ice edge [km]
22/10
24/10
26/10
28/10
30/10
01/11
03/11
(b)
60 km from edge
C_i = 10%
Grease/frazil
(c)
250 km from edge
C_i = 50%
Pancake/brash
(d)
340 km from edge
C_i = 0%
Open water
(e)
430 km from edge
C_i = 100%
Consolidated
pdf
T_{sk} [°C]

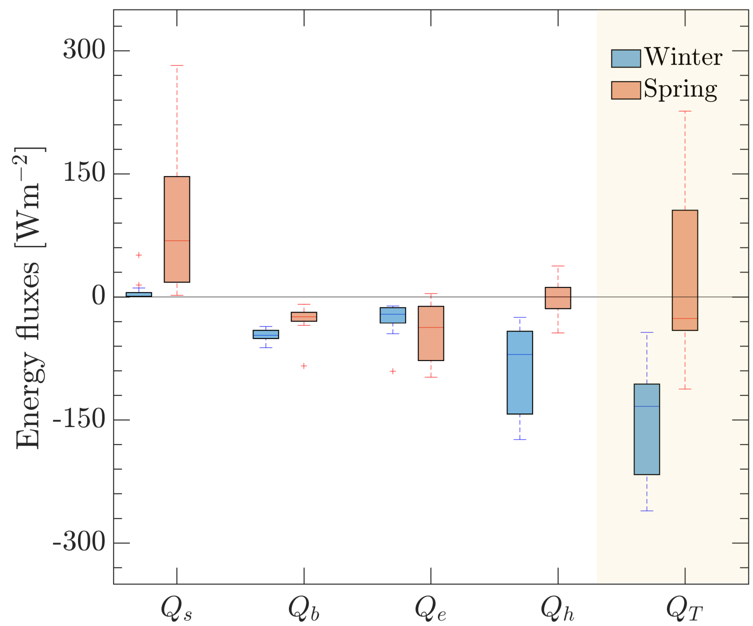

Winter
Spring
Energy fluxes [Wm^{-2}]
300
150
0
-150
-300
Q_s
Q_b
Q_e
Q_h
Q_T

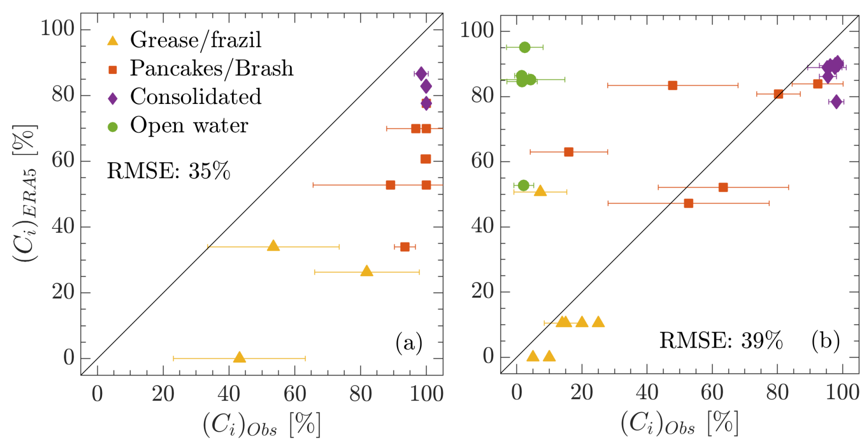

Grease/frazil
Pancakes/Brash
Consolidated
Open water
RMSE: 35%
(a)
RMSE: 39%
(b)
$(C_i)_{ERA5}$ [%]
$(C_i)_{Obs}$ [%]
0
20
40
60
80
100

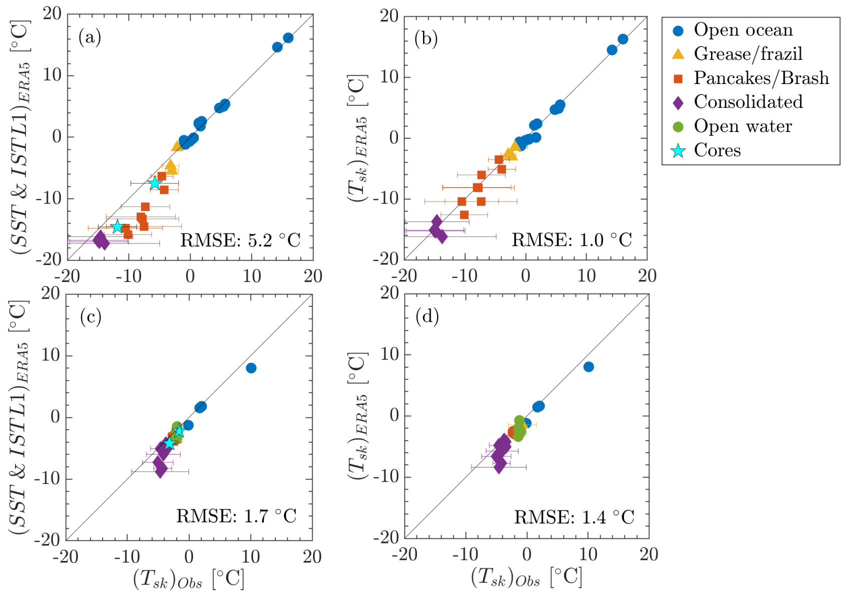
(a)
(b)
(c)
(d)
Open ocean
Grease/frazil
Pancakes/Brash
Consolidated
Open water
Cores
RMSE: 5.2 °C
RMSE: 1.0 °C
RMSE: 1.7 °C
RMSE: 1.4 °C
$(SST\ \&\ ISTL1)_{ERA5}$ [°C]
$(T_{sk})_{ERA5}$ [°C]
$(T_{sk})_{Obs}$ [°C]

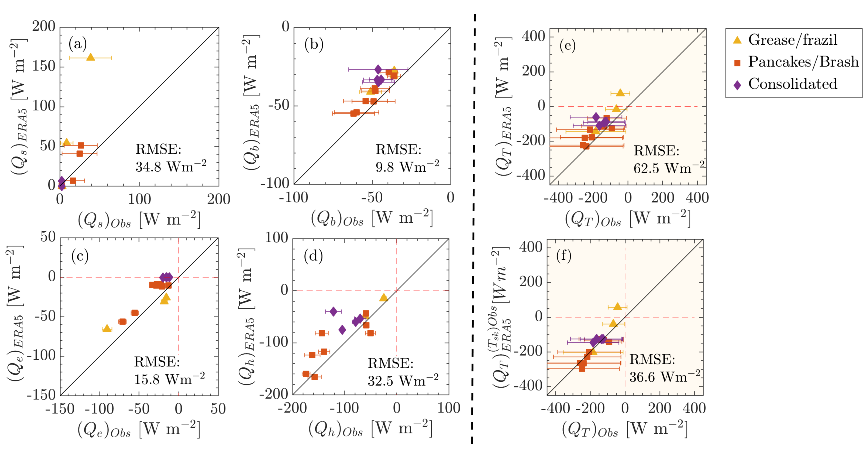
(a)
(b)
(c)
(d)
(e)
(f)
Grease/frazil
Pancakes/Brash
Consolidated
RMSE: 34.8 Wm^{-2}
RMSE: 9.8 Wm^{-2}
RMSE: 15.8 Wm^{-2}
RMSE: 32.5 Wm^{-2}
RMSE: 62.5 Wm^{-2}
RMSE: 36.6 Wm^{-2}
$(Q_s)_{ERA5}$ [W m^{-2}]
$(Q_s)_{Obs}$ [W m^{-2}]
$(Q_b)_{ERA5}$ [W m^{-2}]
$(Q_b)_{Obs}$ [W m^{-2}]
$(Q_e)_{ERA5}$ [W m^{-2}]
$(Q_e)_{Obs}$ [W m^{-2}]
$(Q_h)_{ERA5}$ [W m^{-2}]
$(Q_h)_{Obs}$ [W m^{-2}]
$(Q_T)_{ERA5}$ [W m^{-2}]
$(Q_T)_{Obs}$ [W m^{-2}]
$(Q_T)_{ERA5}^{(T_{sk})Obs}$ [Wm^{-2}]

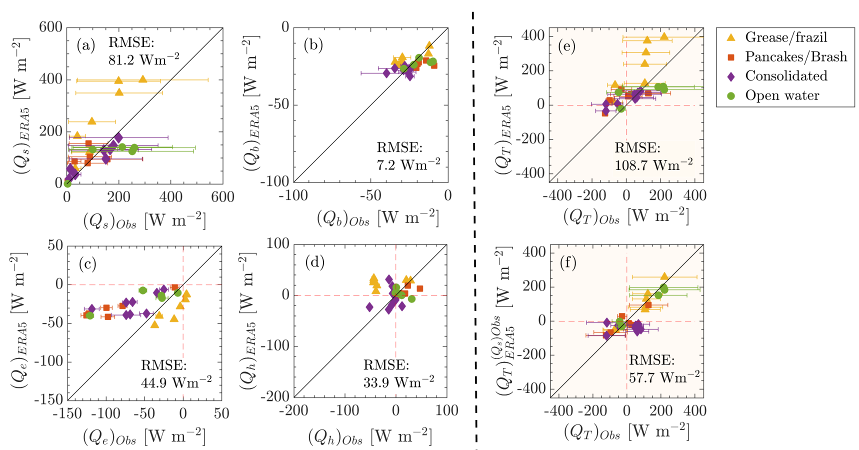
(a)
(b)
(c)
(d)
(e)
(f)
Grease/frazil
Pancakes/Brash
Consolidated
Open water
RMSE: 81.2 Wm^{-2}
RMSE: 7.2 Wm^{-2}
RMSE: 44.9 Wm^{-2}
RMSE: 33.9 Wm^{-2}
RMSE: 108.7 Wm^{-2}
RMSE: 57.7 Wm^{-2}
$(Q_s)_{ERA5}$ [W m^{-2}]
$(Q_s)_{Obs}$ [W m^{-2}]
$(Q_b)_{ERA5}$ [W m^{-2}]
$(Q_b)_{Obs}$ [W m^{-2}]
$(Q_e)_{ERA5}$ [W m^{-2}]
$(Q_e)_{Obs}$ [W m^{-2}]
$(Q_h)_{ERA5}$ [W m^{-2}]
$(Q_h)_{Obs}$ [W m^{-2}]
$(Q_T)_{ERA5}$ [W m^{-2}]
$(Q_T)_{Obs}$ [W m^{-2}]
$(Q_T)_{ERA5}^{(Q_s)Obs}$ [W m^{-2}]

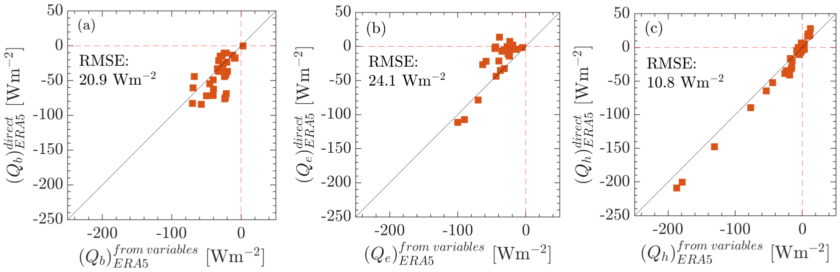
(a)
RMSE:
20.9 Wm^{-2}
$(Q_b)^{direct}_{ERA5}$ [Wm^{-2}]
$(Q_b)^{from\ variables}_{ERA5}$ [Wm^{-2}]
(b)
RMSE:
24.1 Wm^{-2}
$(Q_e)^{direct}_{ERA5}$ [Wm^{-2}]
$(Q_e)^{from\ variables}_{ERA5}$ [Wm^{-2}]
(c)
RMSE:
10.8 Wm^{-2}
$(Q_h)^{direct}_{ERA5}$ [Wm^{-2}]
$(Q_h)^{from\ variables}_{ERA5}$ [Wm^{-2}]
50
0
-50
-100
-150
-200
-250
-200
-100
0

High-resolution thermal imaging in the Antarctic marginal ice zone: Skin temperature heterogeneity and effects on heat fluxes

Ippolita Tersigni[1], Alberto Alberello [2], Gabriele Messori[3,4], Marcello Vichi[5,6], Miguel Onorato[7,8], and Alessandro Toffoli[1]

[1]Department of Infrastructure Engineering, The University of Melbourne, Parkville, VIC 3010, Australia
[2]School of Mathematics, University of East Anglia, NR4 7TJ, Norwich, United Kingdom
[3]Department of Earth Sciences and Centre of Natural Hazards and Disaster Science (CNDS), Uppsala University, Uppsala, Sweden
[4]Department of Meteorology and Bolin Centre for Climate Research, Stockholm University, Stockholm, Sweden
[5]Department of Oceanography, University of Cape Town, Cape Town, South Africa
[6]Marine and Antarctic Research centre for Innovation and Sustainability, University of Cape Town, Cape Town, South Africa
[7]Dipartimento di Fisica, Università degli Studi di Torino, Via Pietro Giuria 1, 10125 Torino, Italy
[8]INFN, Sezione di Torino, Via Pietro Giuria 1, 10125 Torino, Italy

Key Points:

- Thermal images of the ocean surface were used to compute heat fluxes over the Antarctic marginal ice zone in winter and spring
- The marginal ice zone was a compound of several ice types with strong thermal gradients in winter and more homogeneous temperature in spring
- The comparison of heat fluxes against reanalyses points towards biases due to the skin temperature in winter and solar radiation in spring

Corresponding author: Ippolita Tersigni & Alessandro Toffoli, `ippolita.tersigni@gmail.com` & `toffoli.alessandro@gmail.com`

Abstract

Insufficient in-situ observations from the Antarctic marginal ice zone limit our understanding and description of relevant mechanical and thermodynamic processes that regulate the seasonal sea ice cycle. Here we present high-resolution thermal images of the ocean surface and complementary measurements of atmospheric variables that were acquired underway during one austral winter and one austral spring expedition in the Atlantic and Indian sectors of the Southern Ocean. Skin temperature data and ice cover images were used to estimate the partitioning of the heterogeneous surface and calculate the heat fluxes to compare with ERA5 reanalyses. The winter marginal ice zone was composed of different but relatively regularly distributed sea ice types with sharp thermal gradients. The surface-weighted skin temperature compared well with the reanalyses due to a compensation of errors between the sea ice fraction and the ice floe temperature. These uncertainties determine the dominant source of inaccuracy for heat fluxes as computed from observed variables. In spring, the sea ice type distribution was more irregular, with alternation of sea ice cover and large open water fractions even 400 km from the ice edge. The skin temperature distribution was more homogeneous and did not produce substantial uncertainties in heat fluxes. The discrepancies relative to reanalysis data are however larger than in winter and are attributed to biases in the atmospheric variables, with the downward solar radiation being the most critical.

Plain Language Summary

The Southern Ocean stores and release more heat than any other latitude band on the planet, making it a major element of the global climate. In the Antarctic, air-sea heat exchange is mediated by the seasonal sea ice cycle, which forms an unsteady and composite interface of several ice types. In-situ measurements are serendipitous in the region and models are poorly constrained. Here, we present a set of high-resolution thermal images of the uppermost ocean layer (skin temperature) and atmospheric variables acquired underway from the icebreaker S.A. Agulhas II in the austral winter and spring. Observations, and heat fluxes derived from them, are compared with reanalysis, which are model predictions adjusted with assimilated observations different from the ones we collected. In winter, the sea ice shows a neat separation between several ice types with sharp gradients of surface temperature. The reanalysis captures the mean skin temperature, but this is due to error compensation, which ultimately leads to inaccuracies in heat fluxes. In spring, sea ice is a disordered mixture of ice types and open water with a homogeneous thermal distribution. Uncertainties in skin temperature have smaller effects on the heat fluxes modelled by the reanalysis, and differences between reanalysis and observations are dominated by biases in solar radiation.

1 Introduction

The Southern Ocean is a major contributor to the global climate system (Huguenin et al., 2022). Its strong westerly winds fuel intense air-sea fluxes of momentum, energy, gas and freshwater at the ocean surface (e.g. Bharti et al., 2019; Landwehr et al., 2021). Forced by vigorous turbulent mixing through the Antarctic circumpolar current, energetic internal waves and some of the fiercest surface waves on Earth, these fluxes contribute to a deep mixed layer, which stretches from ≈100 m in the austral summer to ≈500 m in austral winter (Dong et al., 2008). This gives the Southern Ocean the capacity to store and release more energy than any other latitude band on the planet, with an annual average energy exchange capacity of ≈30 $\mathrm{Wm^{-2}}$ (Lytle et al., 2000). In comparison, the Arctic ocean has an average energy exchange of ≈3 $\mathrm{Wm^{-2}}$ (Krishfield & Perovich, 2005).

The energy balance combines the intake of shortwave radiation (Q_s) originating from the sun, the net longwave radiation (Q_b), which is the difference between the downward radiation from the atmosphere and the upwelling radiation from the ocean, and the latent (Q_e) and sensible (Q_h) turbulent heat fluxes (Talley, 2011). At high latitudes, the energy budget is complicated by the strong seasonal cycle of Antarctic sea ice (e.g., Dieckmann & Hellmer, 2010; Bourassa et al., 2013; Yu et al., 2017; Landwehr et al., 2021, among others). By insulating the upper ocean from the lower atmosphere, sea ice enhances surface albedo, which changes from ≈10% in open water to ≈20% in young ice to ≈60% in first year ice (Dieckmann & Hellmer, 2010). This fraction increases up to ≈90% in the presence of snow caps (Talley, 2011; R. A. Massom et al., 1998). The absorption of downward solar radiation varies strongly across the seasons. It exceeds 200 Wm^{-2} in an almost ice-free ocean during the austral summer and it drops by one order of magnitude ($Q_s \approx 10$ Wm^{-2}) during autumn and winter (Yu et al., 2017).

The net longwave radiation depends primarily on the temperature of the uppermost layer of the ocean surface (skin temperature; Talley, 2011), which has no heat capacity and, hence, responds instantaneously to changes in radiative (and turbulent) forcing. As the upwelling radiation is generally greater than the downward counterpart, the net radiation represents a loss of energy from the ocean with an annual average of ≈ -50 Wm^{-2} across the Southern Ocean. The mixture of sea ice and open water fractions close to freezing temperature in the Antarctic region produces a markedly colder ocean surface, which enhances the net longwave radiation flux up to ≈50-60% relative to the annual average (Yu et al., 2017).

The primary source of energy loss is represented by the latent and sensible fluxes, which contribute to energy transfer through the evaporation of ocean water (or sublimation of sea ice) and the thermal vertical gradient between ocean and atmosphere, respectively. The former is the dominant component during summer with an average of ≈ -100 Wm^{-2}, while sensible fluxes vary across zero as the thermal gradient is at its minimum. During winter, the contribution of the latent flux eases (Yu et al., 2017). On the contrary, the sensible flux grows, driven by a sharp thermal contrast (this is exacerbated in gaps between ice floes, leads in pack ice, water ponds and polynyas, where ΔT can be up to $\approx$ 20–40°C during winter; Untersteiner, 1964), which enhances turbulent mixing in the atmospheric boundary layer (Monin & Obukhov, 1954). Contributions can be ≈ -150 Wm^{-2} (e.g. Kottmeier & Engelbart, 1992; Yu et al., 2017), making the sensible fluxes the major component of energy loss during sea ice seasons (Lytle et al., 2000; Yu et al., 2017). There is a significant regional variability across the Antarctic, though, which is not well quantified yet (McPhee et al., 1996; Lytle et al., 2000).

Despite some observational evidence, dynamics of radiative and turbulent fluxes remain elusive in the ice-covered ocean (Andreas et al., 2010; Bourassa et al., 2013), especially in the marginal ice zone (MIZ), i.e. the transition region of unconsolidated sea ice that connects the ice-free sub-Antarctic with the Antarctic pack ice (e.g. Alberello et al., 2019, 2022; Vichi et al., 2019; Vichi, 2022). Driven by atmospheric and oceanic forcing (Gryschka et al., 2008; Vichi et al., 2019; Alberello et al., 2020; Womack et al., 2022; Alberello et al., 2022), the MIZ is a mosaic of open water fragments and several sea ice types, comprising of grease, frazil, pancakes, brash and compact ice, with variable thickness of few tens of centimetres and concentration spanning 10-100% (e.g Alberello et al., 2019, 2022; Vichi, 2022; Brouwer et al., 2022). These inhomogeneities contribute to a complicated distribution of the ocean skin temperature (e.g. R. Massom & Comiso, 1994; Lytle et al., 2000; Bourassa et al., 2013), which is the single, most important constraint for energy losses at high latitudes (Lytle et al., 2000; Zwally et al., 2002; Dieckmann & Hellmer, 2010; Bourassa et al., 2013; Horvat & Tziperman, 2018).

A comprehensive figure of the sea ice fraction and skin temperature across the Antarctic can be obtained by satellite remote sensing. Data are sampled over large footprints of approximately 25×25 km with temporal resolutions ranging from 12 to 48 hours. Although large scale averages can be reliable (Fan et al., 2020), the coarse spatial and temporal resolutions are a source of uncertainty as they are not sufficient to detect the smaller spatial and sub-daily scale variability of the Antarctic MIZ (e.g. Kwok et al., 2003; Merchant et al., 2019; Vichi et al., 2019; Alberello et al., 2019, 2020; Womack et al., 2022). Furthermore, surface heterogeneity within the footprint produces signal noise (Rasmussen et al., 2018). Sensors are also susceptible to atmospheric properties such as cloud cover, which limits data availability (O'Carroll et al., 2019; Li et al., 2020). In-situ observations of sea ice concentration and surface temperature, which would underpin calibration and validation of remotely sensed products, are serendipitous in the Antarctic MIZ (Bourassa et al., 2013; Lytle et al., 2000; Skatulla et al., 2022), despite a large number of ship-based measuring campaigns taking place every year (Schmale et al., 2019).

The limited availability of in-situ data is also a challenge for the calibration and validation of numerical models and reanalysis products (Bourassa et al., 2013). Biases in energy fluxes are within ≈10–40 Wm^{-2} (Yu et al., 2019) and escalate into uncertainties in sea ice thermodynamics and, hence, estimates of critical properties such as concentration and thickness (e.g. Rasmussen et al., 2018; Hall et al., 2015; Worby et al., 2008; Horvat, 2021). Interestingly, errors in shortwave and longwave radiations tend to cancel each other (Yu et al., 2019). Therefore, biases in the total energy budget are driven by uncertainties in turbulent fluxes (Liu et al., 2011).

Here we report in-situ measurements of sea ice concentration and surface temperature in the Antarctic MIZ during austral winter and spring. Observations were acquired using a high-speed and high-definition infrared (IR) camera, which captures the temperature of the uppermost (skin) surface layer and resolves the centimetre scale thermal inhomogeneity of the ocean surface (Fig. 1). Data are used to quantify the spatial variability of the sea ice concentration and skin temperature in the MIZ. Complemented by routine observations of atmospheric variables, thermal imaging is used to derive energy fluxes and assess effects of surface heterogeneity on the energy losses. Reanalysis data from the ERA5 archive (Hersbach et al., 2020) are compared against in-situ data to assess effects of small scale variance on key oceanic variables and uncertainties in energy fluxes.

2 Field measurements

In-situ measurements were conducted onboard the icebreaker S.A. Agulhas II, during two expeditions to the Antarctic MIZ in the Eastern Weddell Sea as part of the Southern oCean seAsonaL Experiment (SCALE 2019; Ryan-Keogh & Vichi, 2022). The first voyage took place in August 2019 to monitor the MIZ during its winter growth. The vessel, which set sail from Cape Town (South Africa), entered the MIZ at approximately 56.5°S and continued along the Greenwich meridian until consolidated sea ice was reached at a latitude of about 58°S (≈200 km from the ice edge; Fig. 1b). The vessel remained in sea ice for two days. The second voyage took place in October and November 2019 to survey the sea ice at the onset of its retreat phase. The vessel entered the MIZ at about 55.8°S, following a southward route. It reached consolidated sea ice at 57.5°S and continued until 59°S (≈300 km from the ice edge; Fig. 1c), before sailing eastwards to collect oceanographic and atmospheric data across a zonal sector spanning from 0° to 24°E (Fig. 1c). Overall, the spring expedition spent 12 days in sea ice.

Ocean surface characteristics were monitored with optical sensors. Surface wave properties and geometrical sea ice characteristics (e.g. floe size) were inferred through a stereo camera system in the visible range installed on the monkey island (details in Alberello et al., 2019, 2022). The skin temperature was surveyed with a *Telops* FAST-IR thermal imaging camera equipped with a 13 mm lens (angle of view of ≈120°). To shield wind, rain and sea spray, it was mounted on an intermediate and less exposed deck at approximately 16 m above sea level. The camera was oriented port-side and inclined of

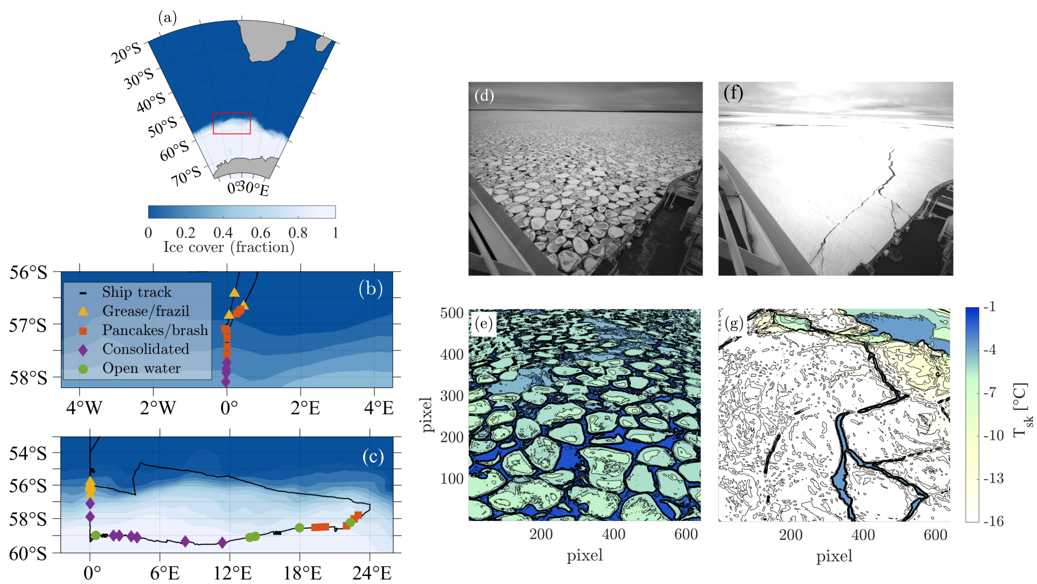

Figure 1. Overview of the expeditions and sample images: (a) Geographical location of the expeditions; (b,c) ship route in the MIZ with indication of monthly sea ice concentration (grading from blue for open waters to white for 100% concentration) and locations of the images and main representative sea ice types for the winter and the spring voyages; (d,e) sample images of pancake ice field in the visible and the infrared range, respectively (fields of view not collocated); (f,g) sample images of consolidated sea ice in the visible and the infrared range, respectively (fields of view not collocated). Sea ice concentration data in (a-c) are extracted from the Near-Real-Time NOAA/NSIDC Climate Data Record of Passive Microwave Sea Ice Concentration; sea ice types are from visual observations on board and from the image inspections.

approximately 40° relative to the horizon. The instrument acquired high-speed and high-definition images in the mid-wave infrared range (MWIR, 3-5 μm) with a resolution of 640×512 pixels and at a minimum rate of 2 frames per second. Images were grouped in 20-minute sequences. Measurements were limited to a maximum of three sequences a day in open waters, but were either continuous or hourly in the MIZ. Sample IR images with the visible counterparts from other not co-located cameras are shown in Figs. 1d-g.

The IR sensor can detect surface temperature between -20 and $+45$°C with a declared accuracy of ±0.005°C. Calibration was performed by the manufacturer and correcting coefficients were applied through an internal process. Performance was checked in the laboratory before and after the expeditions by measuring the (known) temperature of a black body. Image distortion due to the wide field of view of the lens was detected during laboratory tests and rectified in post-processing.

The output image provided the skin temperature at each pixel, from which standard statistics such as the probability density function (pdf), related moments and observation ranges in the form of two times the standard deviation were derived for each sequence. Furthermore, by relying on the freezing temperature, the open water fraction was isolated and the sea ice concentration was estimated. The freezing temperature (T_f) varied with salinity and it ranged from -1.86 to -1.87 °C during the expeditions (cf. Millero, 1978). For the estimate of sea ice concentration, the median value of $T_f = -1.865$ °C was used. To avoid sample overlaps and to ensure the statistical independence of the records only one thermal image every 10 seconds was selected. High humidity rates, haze, and fog interfered with the infrared signal, returning unreliable temperature readings. IR images obtained during these conditions were excluded, noting that these conditions affected primarily data in the open water. Overall, a total of 18 sequences were analyzed for the winter expedition and 82 for the spring one. Despite the inclination of the camera, the field of view still included records of surface temperature at far distances, the accuracy of which is questionable. Hence, the analysis was confined to a window of 640×200 pixels, which coincides with the portion of image closer to the ship. The working window defines a physical footprint of approximately 30×30 m, with a spatial resolution of roughly 0.05 m. A 20-minute sequence covered an overall swath of $\approx 30\,\mathrm{m} \times 3$ km.

The data set was complemented with standard atmospheric variables, including wind speed, air temperature, saturated and specific humidity, and solar radiation through the photosynthetically active radiation (PAR). These were acquired underway from the automatic met-station, which was operated by the South African Weather Service (Ryan-Keogh & Vichi, 2022). Furthermore, sea ice temperature was retrieved from cores extracted at a few stations in the MIZ (Omatuku Ngongo et al., 2022; Audh et al., 2022; Skatulla et al., 2022; S. Johnson et al., 2023). Samples were taken directly from undisturbed compact sea ice and from pancakes lifted onto the ship deck. Temperature was measured immediately after coring, to minimise alterations. Routine visual observations of sea ice (Hepworth et al., 2020), including concentration and type, were recorded following the Antarctic Sea Ice Processes and Climate (ASPeCt) protocol (Worby & Comiso, 2004), throughout the time spent in the MIZ.

3 Computation of surface energy fluxes

There are several empirical formulae for estimating surface energy fluxes. Herein, those proposed in Talley (2011) are used.

The downward shortwave (solar) radiation (Q_{s_d}) was measured as PAR on the ship and estimated following the method in McCree (1972). The portion of solar radiation absorbed by the ocean surface is computed as

$$Q_s = Q_{s_d}(1-\alpha), \tag{1}$$

where α is the albedo of the individual surface components (ocean and sea ice) extrapolated from Table 5 in Brandt et al. (2005) as a function of season, latitude and longitude.

The net longwave radiation is calculated as

$$Q_b = \epsilon\sigma_{SB}T_{sk}^4(0.39 - 0.05e^{1/2})(1 - kC^2) + 4\epsilon\sigma_{SB}T_{sk}^3(T_{sk} - T_A), \tag{2}$$

where $\epsilon = 0.98$ is the emittance of sea surface (Talley, 2011); $\sigma_{SB} = 5.6687\times10^{-8}$ Wm^{-2}K^{-4} is the Stefan-Boltzmann constant; T_{sk} and T_A are the ocean skin and air temperature, respectively; $k = 0.67$-0.75 is a latitude-dependent cloud cover coefficient (J. H. Johnson et al., 1965); C is the fractional cloud cover, which was derived from collocated satellite observations as it was not measured directly; and e is the water vapor pressure, which is the product of saturated vapor pressure (e_s) and the relative humidity (RH; Bechtold, 2009). Values for e_s are determined as (Buck, 1981)

$$e_s = 6.1121\exp\left[\left(18.678 - \frac{T_A}{234.5}\right)\left(\frac{T_A}{257.14 + T_A}\right)\right] \tag{3}$$

in open water and

$$e_s = 6.1115\exp\left[\left(23.036 - \frac{T_A}{333.7}\right)\left(\frac{T_A}{279.82 + T_A}\right)\right] \tag{4}$$

in sea ice.

The latent heat flux (Q_e) is estimated as

$$Q_e = \rho L C_e u(q_s - q_a), \tag{5}$$

where L is the latent heat of evaporation in open water (2260 KJ kg^{-1}) and sublimation in sea ice (2838 KJ kg^{-1}); $\rho = 1.3$ kg m^{-3} is the average air density; u is the wind speed; q_s is the saturated specific humidity at the surface temperature; and q_a is the specific humidity. It is assumed that turbulent mixing does not change with height in the atmospheric boundary layer. Therefore, the transfer coefficient for latent heat C_e is set as a vertically invariant scaling parameters, which is defined as $C_e = 1.20\times10^{-3}$ (Smith, 1988). An alternative approach to evaluate C_e refers to the roughness lengths of momentum, temperature and moisture (see e.g. Andreas et al., 2010; Biri et al., 2023). Relative to the vertical invariant scaling, though, this latter approach does not lead to significantly different values (see Appendix A).

The sensible heat flux (Q_h) is computed as

$$Q_h = \rho c_p C_h u(T_{sk} - T_A), \tag{6}$$

where $c_p = 1004$ KJ kg^{-1} K^{-1} is the specific heat capacity of air at constant pressure. With a vertically invariant scaling approach, the transfer coefficient for sensible heat is expressed as $C_h = 1.0 \times 10^{-3}$ (Talley, 2011).

As the ocean in the MIZ is a composite of two main surfaces, the fluxes were computed separately for sea ice and open water partitions (the mosaic approach; Andreas et al., 2010). The overall flux emerging from the heterogeneous surface is estimated through a weighted average, where the weight is expressed as a function of the sea ice concentration C_i. For a generic component of the energy budget (labeled as Q_g), the resulting flux is expressed as:

$$Q_g = C_i(Q_g)_{ice} + (1 - C_i)(Q_g)_{water}. \tag{7}$$

The total heat flux (Q_T) at the ocean surface is the sum of all radiative and turbulent fluxes:

$$Q_T = Q_s + Q_b + Q_e + Q_h. \tag{8}$$

4 In-situ sea ice observations from IR images

4.1 Reliability of skin temperature from IR images

The skin temperature from IR images was tested against satellite data and core measurements. In the the open ocean, the benchmark skin temperature was retrieved from several satellite-borne sensors available through the Near-Real-Time NOAA/NSIDC Climate Data Record of Passive Microwave Sea Ice Concentration database (Chin et al., 2017). Collocation was enforced by clustering and averaging the data over grids with side of 0.25 degrees and centered on ship's positions; a 50% overlap between consecutive locations was considered. In the MIZ, only the skin temperature of the sea ice fraction was considered and it was compared against co-located measurements of near-surface temperature from ice cores (see §2). Co-located observations of sea ice skin temperature from satellite-born infrared sensors were not available due to cloud cover.

The data comparison is presented in Fig. 2. Observation ranges, shown in the form of errors bars, were small (and hidden by the symbols) for the open ocean measurements, indicating a homogeneous distribution of skin temperature in the grid box. An evident variability was found in the MIZ, denoting a more heterogeneous temperature distribution of sea ice (see §4.2).

The open ocean skin temperature from the IR camera was in good quantitative agreement with satellite sensors. The sea ice skin temperature was also consistent with ice core measurements. However, there is an evident bias, yet confined within the observation range, with the IR camera returning a colder surface temperature. Whereas the camera detects the uppermost surface layer, the ice core measurements refer to a less exposed and, hence, warmer sub-layer.

4.2 Skin temperature and sea ice concentration

The bulk weighted average of the skin temperature from the IR images is presented in Figs. 3 and 4 as a function of time and distance from the ice edge for winter and spring, respectively. The weighted average mediates sea ice and open water partitions and is computed as:

$$T_{sk} = C_i (T_{sk})_{ice} + (1 - C_i)(T_{sk})_{water}, \tag{9}$$

where $(T_{sk})_{ice}$ is the average sea ice skin temperature and $(T_{sk})_{water}$ is the open water counterpart. The ice edge is defined as the northernmost latitude where sea ice concentration is 10%.

During the winter expedition, a sharp drop of air temperature was observed while sailing into the MIZ (along a southward route; Fig. 1b), which corresponded to a smooth drop of skin temperature (Fig. 3a). Conversely, an increase of temperature was reported on the way out. The outermost samples, located within 100 km from the edge, were taken in partially ice covered waters, with concentrations in the range 40-90%. From the image inspection and observations onboard, the sea ice comprised new ice formation such as grease, frazil and, more sporadically, pancakes. The skin temperature varied from a maximum of $-2°$C to a minimum of $-4°$C; air temperature was $\approx -5°$C. Despite the narrow range, the pdf displays two close, and yet evident, peaks on either side of the freezing temperature, separating sea ice from open water fractions (Fig. 3b). The samples in the band 100-200 km from the ice edge were dominated by pancakes (thickness of 0.3-0.8 m). The sea ice fraction increased to 90-100% and the skin temperature was $-10°$C $< T_{sk} < -5°$C. A notable vertical gradient was reported with air temperature being approximately 5°C colder than the skin temperature. At 110 km, the pdf showed a well developed bimodality (Fig. 3c). The ice-type population around the freezing temperature was equivocal as it mixed water and grease/frazil ice. However, the peak emerging at $\approx -5°$C represented pancake ice distinctly. Whereas the separation between the two peaks was net, there was a large number of data points between the peaks. These rep-

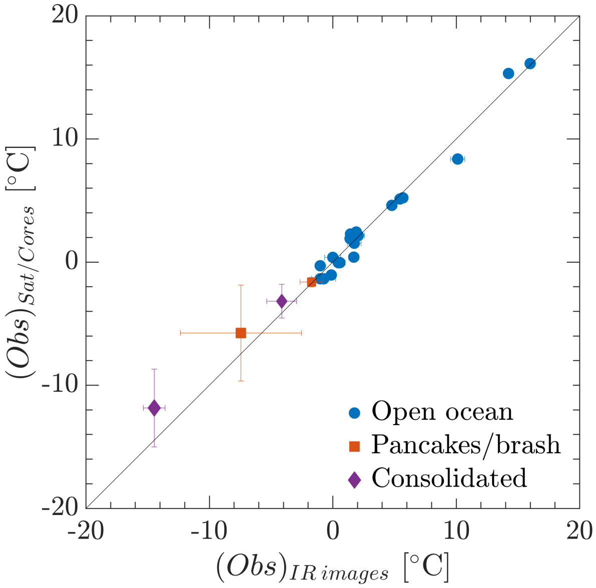

Figure 2. Thermal imaging against satellite data and core measurements. For open ocean conditions, observations of the sea surface skin temperature from the IR camera are compared against skin temperature from satellite sensors. In the MIZ (pancake/brash and consolidated ice), the sea ice skin temperature from the IR camera are compared against sea ice near-surface temperature (i.e. 2.5 cm below the surface) from ice cores. The error bars represent the observation ranges.

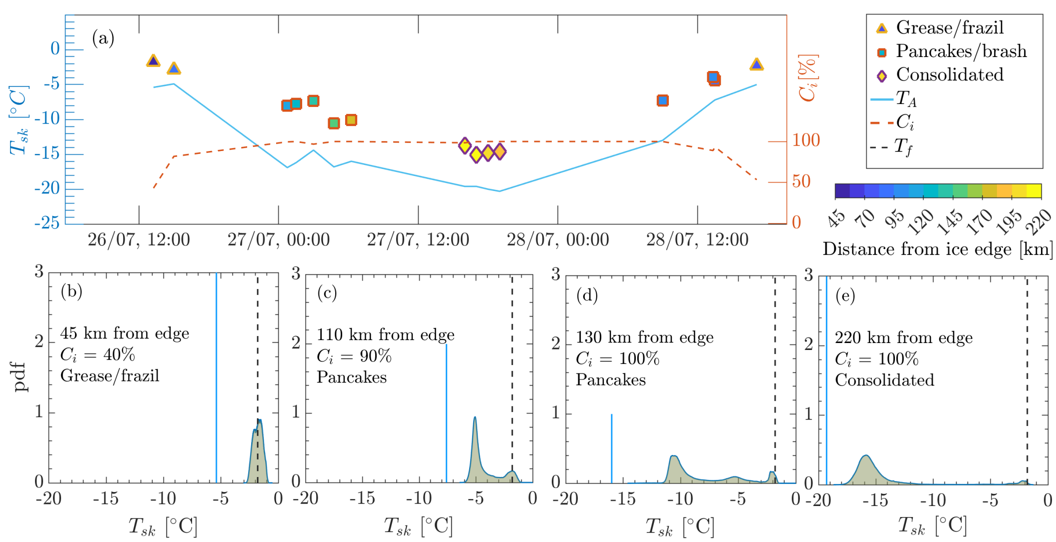

Figure 3. Skin temperature in the marginal ice zone during the winter expedition (Fig. 1b): (a) bulk weighted average as a function of time (x-axis) and distance from the edge (color code); (b-e) examples of probability density functions of skin temperature at various distances from the ice edge. As reference, air temperature (T_A), freezing temperature (T_f) and sea ice concentration (C_i) are reported.

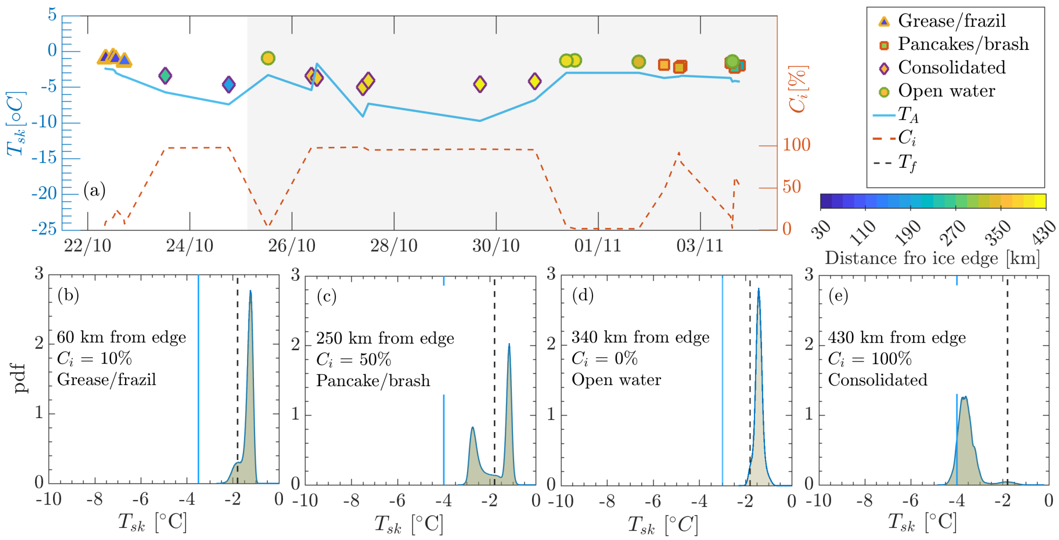

Figure 4. As in 3 but for the spring expedition (Fig. 1c). Data within the grey shaded area in (a) refer to observations taken along the eastward route (longitudes 0-24°E; cf. Fig. 1c).

resent a mixture of grease and frazil ice, which formed in the interstitial space (see Figs. 1d,e). Further South in the pancake region (Fig. 3d), the skin temperature of sea ice cooled down, denoting more mature pancake floes. A neat separation between ice types confers the pdf a characteristic trimodal form: the peak at -10.5°C represent pancakes; the peak at -5.5°C is grease/frazil ice; and the peak around freezing temperature is a mix of open water and grease/frazil ice. Over ≈200 km from the edge, the sea ice cover was ≈ 100%, with thickness of ≈ 1 m, which originated from pancake welding. Leads of variable lengths and width were common in the region (Figs. 1f,g). The thermal vertical gradient remained approximately 5°C. The pdf resumes a bimodal feature in consolidated sea ice at 220 km from the edge (Fig. 3e). Sea ice skin temperature is centred at -16°C, while warmer water emerging from leads gives rise to a lesser peak at ≈ -2.5°C. It is worth noting that no sea ice of any form was observed in the openings. Hence, the cold temperature in the leads is attributed to super-cooled water (cf. Haumann et al., 2020).

In spring (Fig. 4), the MIZ exhibited a more variable composition. Throughout the spring expedition, the air temperature was consistently colder than the skin temperature, with a vertical gradient of $\approx 2-3$°C. The image sample from the outermost region was characterised by scattered formation of grease ice with C_i <30%. This region extended for ≈150 km from the edge (about half way through the southward route; see Fig. 1c). The significant weight of open water fractions in this band resulted in a stable skin temperature with distance from the edge, which was consistently above freezing. The pdf is markedly narrower than in winter (Fig. 4b) with a dominant open water mode at ≈ -1.36°C. A smaller second peak centred at about the freezing temperature is also visible. The identification of the ice type from this secondary peak is ambiguous as it is in between the skin temperature of water and the grease/frazil ice temperature found in winter. The sample taken from the region between 150 and 300 km from the edge (second half of the southward route) was consistently dominated by compacted ice with leads ($C_i \approx 100$%). Although a large open water fraction was reported at the beginning of the eastward route (cf. Fig. 1c), compact ice remained the prevailing ice type along the first half of the eastward transect (0-12° E; data within 26/10 and 30/10 in Fig. 4a), noting the vessel also sailed further South until about 450 km from the edge. The averaged skin temperature was ≈ -5° C. The pdf is dominated by the sea ice partition with a secondary peak just above the freezing temperature denoting open water from leads (Fig. 4e). Further East (longitudes 12-24°E; Fig. 1c), the average skin temperature increased to ≈ -2°C. This section of the transect followed a northeasterly route, moving from about 450 to 250 km from the ice edge. Sea ice conditions changed into a disarranged mixture of new pancake formations, pancake-like floes from broken-up consolidated ice, and occasional large leads and open water fractions of size up to approximately 10 km, as visually detected from the images and the onboard observations (Hepworth et al., 2020). In this cluster of images, the sea ice concentration was highly variable between 0-100% (see data within 01/11 and 03/11 in Fig. 4a). The pdf shows evident bimodality in region dominated by pancake-like floes (Fig. 4c) and a distinctive unimodality centered at temperature above freezing in regions of open water (Fig. 4d).

4.3 Heat fluxes

The heat fluxes computed from eqs. 1-8 for all the acquired image clusters are summarised in Fig. 5. The absorbed shortwave radiation is small over winter as the upper interquartile range does not exceed 5 Wm^{-2}. Sporadic records acquired at solar noon reached values up to $\approx$50 Wm^{-2}. In spring, the shortwave radiation increased, but so did the spread with the interquartile range $\approx 15 - 150$ Wm^{-2}, noting that the lowest values are associated to nighttime or periods of extended cloud coverage and the largest coincide with observations at solar noon. The net longwave radiation exhibited a similarly narrow spread in both seasons. Energy losses varied between -60 and -30 Wm^{-2} in winter and -40 and -10 Wm^{-2} in spring.

Also the latent flux remained small in winter and with a narrow spread from -50 to -10 Wm^{-2}. It instead increased in spring and showed a larger variability spanning from -100 to 0 Wm^{-2}, primarily due to the higher changes in humidity (cf. Fig. B1).

The sensible flux was the most substantial energy loss in winter with magnitude spanning from -150 to -30 Wm^{-2} due to large thermal gradient between the ocean and the atmosphere. Conversely, it was less intense and both positive and negative in spring -30 Wm^{-2} and 20 Wm^{-2} owing to the smaller gradient (Fig. 4a).

The total energy flux in winter was negative, mostly due to the low shortwave radiation flux and the large negative latent heat flux. This is expected during the sea ice advance period. In spring, the median was also negative; the spread was large spanning from -120 to 250 Wm^{-2} but skewed towards the negative values. This indicates a possible sea ice growth phase that coexisted with the onset of breakup during spring, particularly explaining the observations of both new pancake formations and brash ice from broken-up compact ice found in the eastern part of the track.

5 Comparison with ERA5 reanalyses

5.1 Reanalysis products and matching with field observations

There are several publicly available climate reanalysis products. Here we adopt the ERA5 data set from the European Centre for Medium-Range Weather Forecasts (ECMWF; Hersbach et al., 2020), which produces hourly variables with a spatial resolution of 0.25°. An intercomparison of air-sea variables and energy fluxes from different reanalysis products in the Southern Ocean is discussed in Liu et al. (2011) and Yu et al. (2019). Assessment against in-situ measurements in the Antarctic MIZ shows that the ECMWF's reanalysis is the most accurate (Yu et al., 2019), motivating the decision to use the ERA5 as benchmark.

For consistency with field observations (§3), basic atmospheric variables were retrieved from ERA5 and applied as input in eqs. (1-8) to estimate radiation and turbulent fluxes. Variables were recovered at ship's locations with compatible reanalysis output times, through linear interpolations between nearby grid points. To build compa-

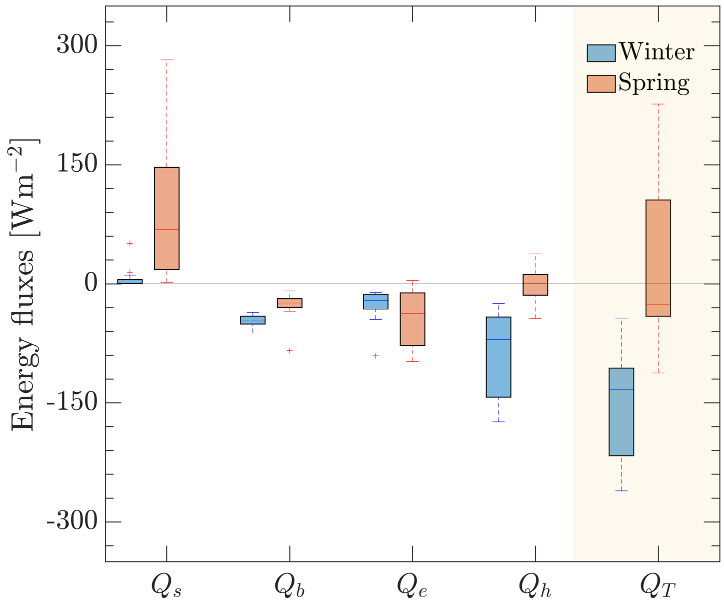

Figure 5. Box-and-whisker plots of the energy flux components (Q_s, Q_b, Q_e and Q_h) and the total budget (Q_T). The boxes represent the interquartile range (25^{th}-75^{th} percentiles); the central mark of the box indicates the median; whiskers extend to the most extreme data points not considered outliers; + symbols are outliers.

rable and collocated field observations, in-situ data falling in the ERA5's grid box of side 0.25° containing the ship's position and within a time window of ±30 minutes relative to the reanalysis were selected and averaged.

In the following, we present the comparison of skin temperature, sea ice concentration, and the resulting fluxes computed from these and other ancillary variables from observations and ERA5. The other atmospheric variables are shown in Appendix B. A further comparison between the estimated fluxes and those obtained directly from ERA5 is presented in Appendix A for completeness.

5.2 Sea ice concentration

The sea ice fraction in the reanalysis was ≈ 35% lower than observed in the IR data (Fig. 6a). This discrepancy is evident for all the ice types seen in the images over a spatial range of more than 200 km, which comprises about 10 pixels of the original satellite data prescribed in ERA5. Interestingly, the assimilated ice fraction was always $C_i \leq$ 80%. Discrepancies are the largest in pancake ice images, where the concentration provided by ERA5 is two-thirds of the observed one. In this region, the satellite algorithm only identified mature and larger pancake floes, but it did not capture the interstitial grease/frazil ice that was detected as ice free. This is in contrast with the conditions reported by Alberello et al. (2019) during winter in the Indian Ocean sector, in which interstitial sea ice between pancake floes was instead identified as ice, resulting in 100%, apparently consolidated ice cover despite the observed substantial wave propagation (Alberello et al., 2022). It is therefore complex to distinguish the winter mixture of pancakes and interstitial ice from space, and satellites return contrasting concentration values from similar surfaces.

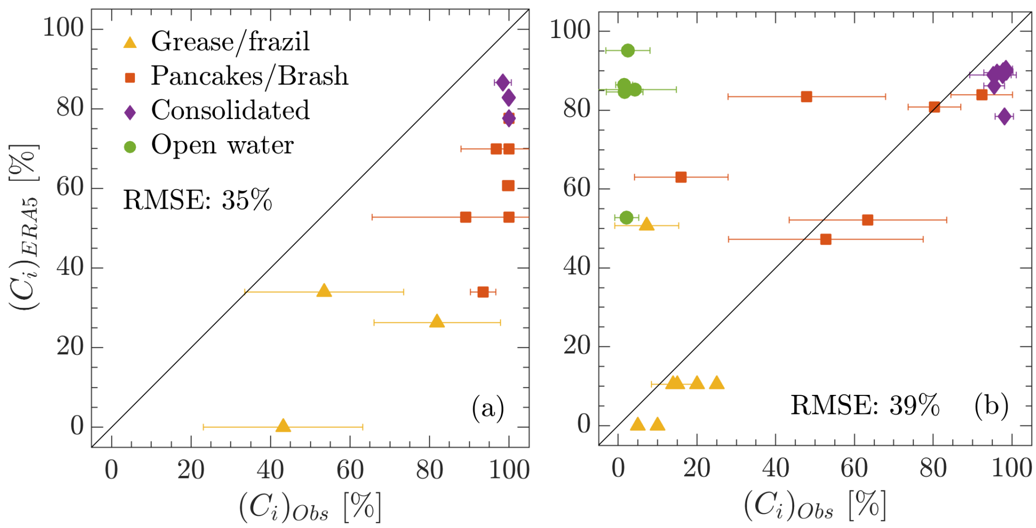

Figure 6. Sea ice concentration from ERA5 versus in-situ observations from IR images for the winter (upper panels) and spring (lower panels) expeditions: (a) winter; and (b) spring. The threshold for partitioning the sea ice fraction in the IR images was the freezing temperature ($T_{fr} = -1.865°$ C). Error bars represents the observation range.

The comparison improves in spring (Fig. 6b). The images containing grease/frazil and consolidated ice (southward transect and first half of the eastward transect—longitude 0-12°E; Fig. 1) were better represented in the ice cover fraction prescribed in ERA5, although there was still a tendency to underestimate the concentration. Data from longitudes 12-24°E along the eastward transect (Fig. 1) showed evident inconsistencies between the reanalysis and in-situ observations. While several data points were captured by ERA5, some others were overpredicted by 30-40%. This region was also complicated by the presence of large openings. These were not detected by the reanalysis, which predicted almost full sea ice coverage instead of 0-5% reported in-situ. The presence of open water patches was the main reason for the large root mean squared error (RMSE) of $\approx$ 40%.

5.3 Skin temperature

In ERA5, the ocean surface is partitioned into sea ice and open water. The skin temperature in sea ice is estimated from the layer one sea ice surface temperature (ISTL1; i.e. the temperature at 3.5 cm depth in bare ice) through the conductivity coefficient, while its open water counterpart is a function of the bulk sea surface temperature (SST, (See details in ECMWF, 2016b)). The overall skin temperature is computed as a weighted average following eq. 9. Since the skin temperature for individual partitions is not available for download, we used ISTL1 and SST in our analysis when considering ice and open water separately.

The comparison with in-situ data is presented in Fig. 7 for winter and spring. Panels (a,c) distinguish the ocean and ice partitions. The in-situ skin temperature of sea ice is compared against ISTL1, which is the only near-surface product available in ERA5, while skin temperature of open ocean is compared against the ERA5 SST. We acknowledge the different depths between in-situ data and ERA5, although it is expected that the thermal gradient between the skin and an immediate sub-layer is confined within 1°C and the sub-layers are warmer than the surface (Talley, 2011; ECMWF, 2016b). In winter, the SST compared well with observations, indicating that differences between skin and sub-layer temperature are indeed minimal. Deviations emerged in the MIZ, depending on the sea ice type. Differences were negligible in grease/frazil ice, while they increased by several degrees in pancake conditions and slightly reduced again in consolidated ice. The overall RMSE in the MIZ was about 4 °C, with a mean bias of -3.5°C (i.e. ISTL1 is colder than observations). This discrepancy is significant because ISTL1 is expected to be equal or warmer than the actual skin temperature of sea ice. The relevance of the error is further confirmed by the core measurements taken at 2.5 cm from the surface, and thus more comparable with ISTL1, which were indeed warmer than the skin temperature of sea ice from the IR images (Fig. 2) and thus also warmer than ISTL1. In spring, in-situ and ERA5 data were more similar, although ISTL1 remained slightly colder than the observed skin temperature (RMSE$\approx$ 1.74°C and mean bias ≈ -1.4°C) and an evident deviation emerged for consolidated sea ice conditions.

The weighted skin temperature computed with eq. 9 in winter improves with respect to the sea ice partition (Fig. 7b), except for a few pancake ice images. The RMSE reduces to $\approx 1.0°$ C. Recalling that the skin temperature mediates sea ice and open water fractions, this improvement is attributed to an artificial effect arising from uncertainties in the sea ice concentration and ISTL1. Excessively cold ISTL1 in ERA5 are counterbalanced by a large fractions of open water, contributing to warming the skin disproportionately. Hence, it is the compensation of errors that justifies the accurate match of skin temperature in Fig. 7b.

In spring, the skin temperature compared relatively well with field data. The error compensation reported in winter is not evident as the more homogeneous temperature distribution attenuates the differences in sea ice concentration (Fig. 6b, with the notable exception of the missing oper water leads). The RMSE remains similar between the partitioned and the weighted skin temperatures, with a mean bias of ≈ -0.9°C.

5.4 Radiative, turbulent and total heat fluxes

The radiative, turbulent and total heat fluxes are reported in Figs. 8 and 9 for the winter and spring expeditions, respectively. In winter, the solar radiation (Q_s) from ERA5 is mostly consistent with observations apart from an evident overestimation by 40-100 Wm^{-2} in regions dominated by grease/frazil and pancake ice, where discrepancies in sea ice concentration exceed 50% (Fig. 6a). The net longwave radiation and turbulent fluxes from the reanalysis show a systematic overestimation: the RMSE is ≈ 9.8 Wm^{-2} for Q_b, $\approx$ 15.8 Wm^{-2} for Q_e and ≈ 32.5 Wm^{-2} for Q_h. Differences are particularly significant for turbulent fluxes as they always exceed the observation range. The ERA5 total flux (negative as dominated by losses) is, to some extent, consistent with the observations. There is an evident overestimation, but this is generally within the relatively large observation range (Fig. 8e). The RMSE of ≈ 62.5 Wm^{-2} is attributed to the underestimation of skin temperature. This is confirmed in Fig. 8f, in which the total energy flux from ERA5 is recomputed using the in-situ skin temperature. This correction reduces the RMSE by about 50%. The substitution of the other atmospheric variables shown in Appendix B produces lesser effects on the total budget than the skin temperature.

In spring (Fig. 9), the main difference is found in Q_s, with the reanalysis overestimating the solar radiation flux by 50-200 Wm^{-2}. Given that the sea ice concentration is mostly well-captured (Fig. 6b, with the exception of some open-water conditions as discussed below), this error cannot be attributed to the ice cover imposed to ERA5. The disagreement comes directly from the downward solar radiation flux that differs by the same magnitude when compared to the ship sensor (see Fig. B1). The solar radiation

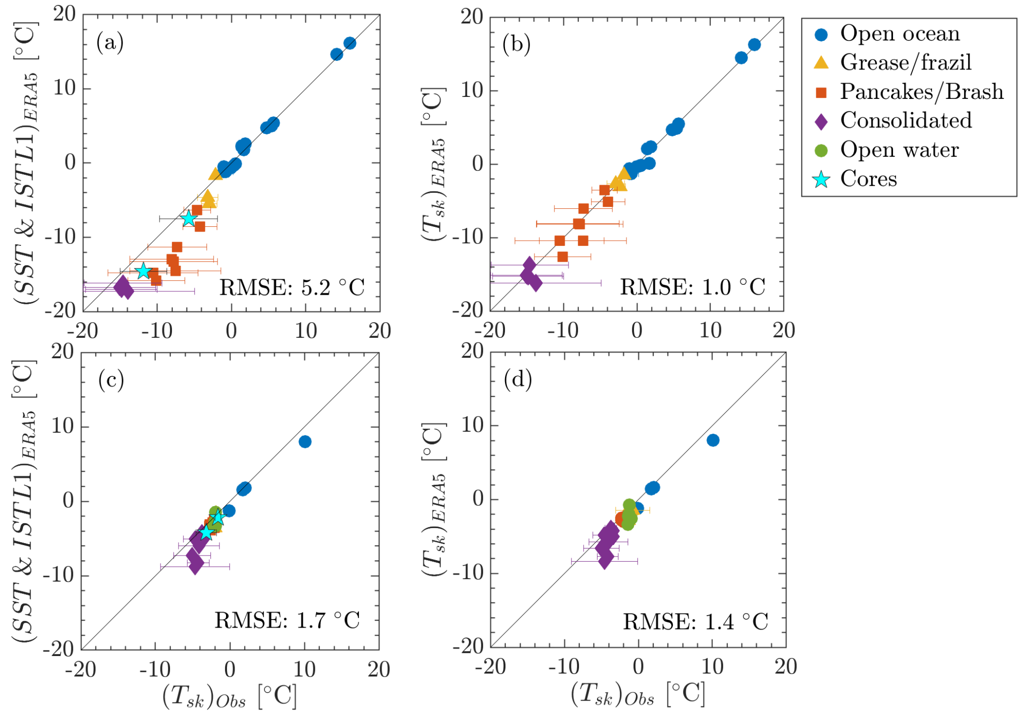

Figure 7. Comparison of surface temperature for the winter (upper panels) and spring (lower panels) expeditions: (a,c) sea ice surface temperature (ISTL1, at 2.5 cm below the surface) in the MIZ and bulk sea surface temperature for open ocean from ERA5 are compared against the sea ice partition of the skin temperature in the MIZ and water skin temperature in the open ocean from IR images; and (b,d) the weighted average overall skin temperature from ERA5 is compared against the IR images counterpart. Error bars represents observation range. The RMSE refer to the portion of data points in the MIZ.

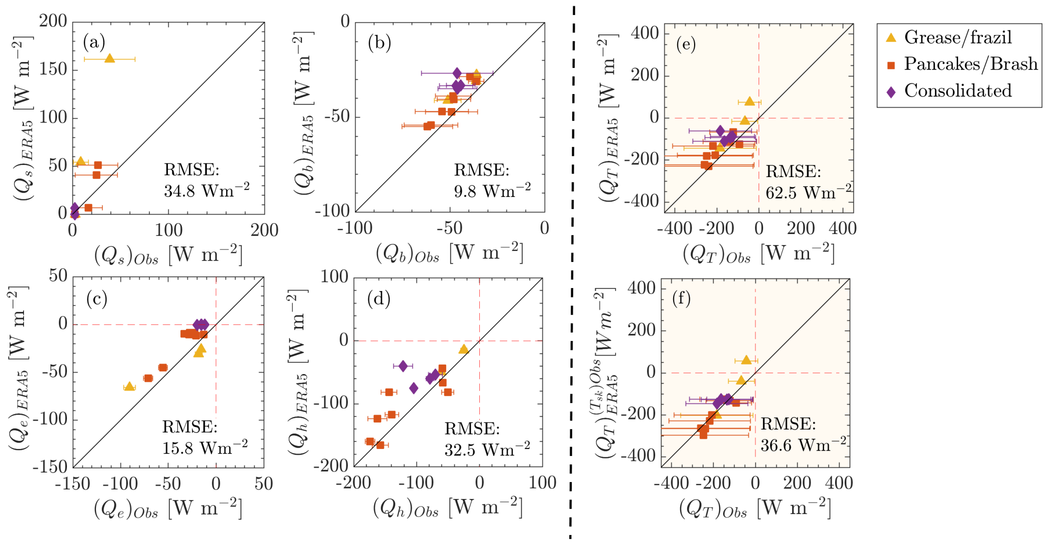

Figure 8. Energy flux components computed using air-sea variables from ERA5 versus estimations based on in-situ observations for the winter (a-d). Total energy flux computed using atmospheric variables from ERA5 (e) and ERA5 forced by in-situ skin temperature (f) versus estimations based on in-situ observations for the winter. Error bars represent observation range.

in summer is known to be affected by inaccuracies in the cloud coverage simulations (e.g. Flato et al., 2014; Yu et al., 2019; Fiddes et al., 2022) and this is confirmed also in spring in this region. Interestingly, there is a small subset of data for which Q_s is underestimated by the reanalysis by ≈ 100 Wm^{-2}. This is instead due to the use of the wrong sea ice surface, because it corresponds to the low-albedo of open water fractions (longitudes 12-24°E of the eastward transect), which are seen as consolidated ice by ERA5. The long-wave radiation (Q_b) and the sensible (Q_h) flux were captured reasonably well with RMSE ≈ 7 and 34 Wm^{-2}, respectively. The scatter is attributed to discrepancies in the skin temperature. The latent heat flux shows a larger spread with an evident underestimation of observations in the sector of mature sea ice conditions and overestimation in grease/frazil ice, with an overall RMSE of ≈ 45 Wm^{-2}. These errors are attributed to inaccuracies in simulating wind speed and the saturated and specific humidities as shown in Fig. B1. Unlike winter, the total budget is dominated by Q_S and most of the locations show an evident energy gain in the reanalysis. Relative to in-situ data, ERA5 has a negative bias with fluxes consistently overestimated (Fig. 9e), noting that there are examples, across all ice types, where reanalysis exhibits gain while loss was reported in the field. A few samples in pancake and open water regions are underestimated. These differences depend on errors in atmospheric variables such as skin temperature, wind speed and humidity (cf. Appendix B). However, the largest impact in spring is due to the inadequate representation of Q_s in ERA5. The recalculated total energy flux in which the in-situ Q_s replaces the ERA5 values is more in agreement with the measurements and reduces the RMSE by approximately 60% (Fig. 9f). Similarly to the winter case, the other substitutions do not produce a similar improvement.

6 Conclusions

High-resolution infrared images of the uppermost layer of the ocean surface were acquired during winter and spring expeditions to the Antarctic marginal ice zone in the Eastern Weddell sea sector. Images provided data on the skin temperature and morphology of the heterogeneous surface, which were eventually converted into sea ice concen-

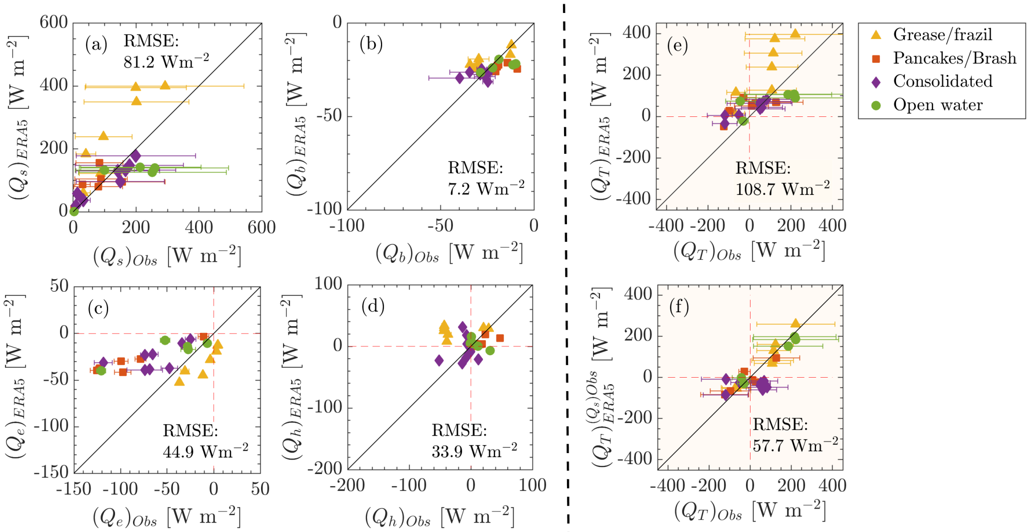

Figure 9. As in Fig. 8 but for the spring expedition; panel (f) shows ERA5 forced by the in-situ intake of solar radiation (Q_S) versus estimations based on in-situ observations.

tration. Combined with other atmospheric variables measured onboard, these were applied to estimate radiative and turbulent heat fluxes over the ice-free and ice-covered ocean portions through bulk formulae and compared with output variables from the ERA5 reanalysis.

In winter, the sea ice cover was an organised compound of several, neatly separated in space, sea ice types. The external region within ≈100 km of the ice edge was dominated by young ice formations, including grease, frazil and newly formed pancakes. This was followed by a region of more mature pancakes between $\approx 100 - 200$ km from the edge, with interstitial spaces occupied by either water or grease/frazil ice. Consolidated sea ice with leads was observed beyond 200 km from the ice margin. IR images revealed sharp inhomogeneities of the skin temperature in the exterior MIZ due to the coexistence of several sea ice type and open water fractions, and a more uniform distribution in consolidated ice. The total energy balance was dominated by losses through the net longwave radiation and turbulent latent and sensible heat fluxes, with the latter being the main contributor by one order of magnitude. Despite a notable variability, which was also reported in one of the few earlier studies on the topic (Lytle et al., 2000), the losses were in the order of -10^2 Wm^{-2}, underpinning the winter sea ice growth.

The ERA5 matches observations of skin temperature reasonably well, despite a tendency to predict a colder surface (a similar small bias was reported in Cerovečki et al., 2022). We found that this apparent agreement is forced by compensation of errors. On one side, the sea ice partition is far colder than observations, while on the other the reanalysis exhibits a smaller sea ice fraction. Open waters result in a significant warming of the skin temperature, hence counterbalancing the colder sea ice skin. Due to this compensation, energy fluxes from ERA5 are ultimately compatible with observations, although biased towards less intense fluxes. These result in a more moderate energy loss than in-situ, which we attribute to the small, yet relevant, uncertainties in skin temperature. To a certain extent, this is also reported in King et al. (2022); Cerovečki et al. (2022), which link it to biases of the downward component of the longwave radiation.

The spring data showed a more homogeneous distribution of skin temperature with less sharp thermal contrast between water and sea ice partitions. Yet, this reflected a

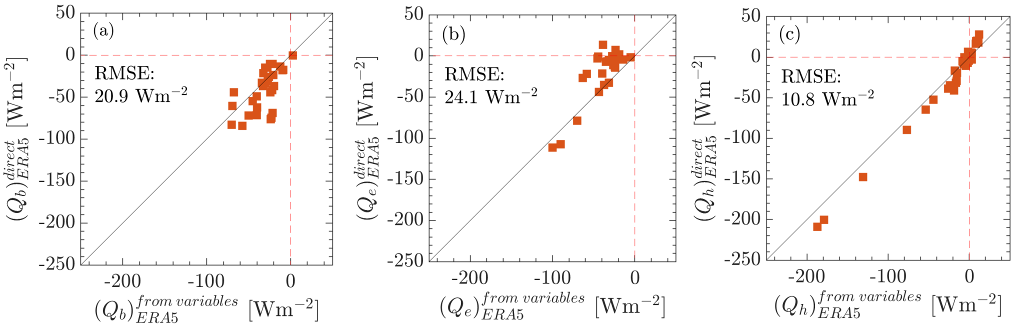

Figure A1. Example of net longwave radiation flux (a), latent heat flux (b) and sensible heat flux (c) estimated from the bulk formulae in eqs. (1-8) with ERA5 air-sea variables as input against those provided directly by ERA5. Data are from a single grid point located along the ship's route at about 150 km from the ice edge and for every day at 12pm of the month of July (2019).

disarrayed sea ice cover, comprising large open water fractions as far as 400 km from the ice edge, young ice formations and more mature sea ice conditions originating from both growth and breakup. Sea ice concentration was erratic and ranged 0-100%, even deep in the sea ice region. Despite an intense intake of solar radiation relative to winter, the total energy fluxes showed a large spread spanning from losses to gains with the distribution skewed towards the former. This substantiates a particularly complex sea ice dynamics in spring, where melt and growth are concurrent.

Reanalysis represents skin temperature well over spring, despite a persistent small cold bias. The error compensation that is reported in winter is not evident. The total energy flux from reanalysis shows a more complicated relationship with observations than in winter. Reanalysis produces a consistent energy gain during the observation period and does not capture the alternation of gains and losses reported in-situ. Our results indicate that the biases in shortwave radiation estimates from ERA5 reported by other authors in summer are the dominant source of error also in spring.

Observations presented herein contribute a step further in our understanding of complex air-sea interaction processes in the Antarctic marginal ice zone, especially in the still largely unexplored winter season. It is essential that such high resolution measurements become routine on voyages to Antarctica across all seasons. This would contribute to a more comprehensive sampling of sea ice in several geographical sectors, providing vital data for unravelling the dynamics driving the sea ice cycle and improving both models and remote sensing products.

Appendix A Vertical invariant scaling and roughness length approach

The ERA5 computes the fluxes using near-surface temperature (SST and ISTL1), other atmospheric variables and transfer coefficients for turbulent fluxes based on characteristic length scales (ECMWF, 2016a). In the main text, the fluxes from ERA5 were computed with the bulk formulae in eqs. (1-8) using the skin temperature and other atmospheric variables from ERA5 as input and transfer coefficients for turbulent fluxes based on a vertical invariant scaling. A comparison between these approaches is presented in Fig. A1 for the winter net longwave radiation, latent, and sensible heat fluxes.

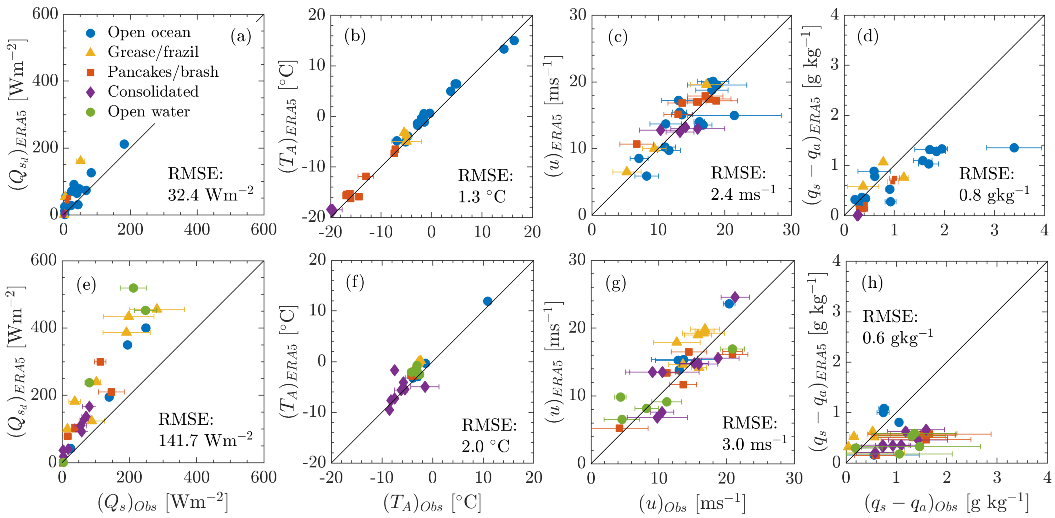

Figure B1. Comparison between in-situ observations from the meteorological station aboard the S.A. Agulhas II and reanalysis from ERA5 for the winter (a-d) and spring (e-h) expeditions: (a-e) downward solar radiation; (b-f) air temperature; (c-g) 10-metre wind speed; and (d-g) the difference between saturated and specific humidity.

Appendix B Other atmospheric variables and comparison with reanalysis

The comparison between in-situ and ERA5 data for other relevant air-sea variables (i.e. downward solar radiation, air temperature, wind speed, and the difference between saturated e specific humidity) is reported in Fig. B1. Note that some basic atmospheric variables such as air temperature and pressure have been assimilated in the ERA5 and, hence, these supporting data are not totally independent from reanalysis. In winter, ERA5 is, to a certain extent, consistent with in-situ observations. However, there is an evident tendency to over estimate downward radiation (RMSE $\approx$ 32 $\mathrm{Wm^{-2}}$) and wind speed (RMSE $\approx$ 4 $\mathrm{ms^{-1}}$). In spring, the downward solar radiation and wind speed are over estimated by the reanalysis with RMSE $\approx$ 112 $\mathrm{Wm^{-2}}$ and 3 $\mathrm{ms^{-1}}$, respectively. The difference between saturated and specific humidity is under estimated in winter and spring (RMSE $\approx$ 0.31 g $\mathrm{kg^{-1}}$). The air temperature is well captured.

Availability statement

Processed data from IR images (skin temperature and sea ice concentration) and supporting atmospheric variables that were used for this study are published in Zenodo and can be access through the link `https://doi.org/10.5281/zenodo.7943559`. ERA5 reanalysis can be downloaded from the Copernicus Climate Change Service (`https://cds.climate.copernicus.eu/#!/home`). The codes used to process thermal imaging and perform the analysis are available upon request to the corresponding authors.

Authors contribution

Conceptualization: IT, AA, MV, MO, AT; Methodology: IT, MV, AT; Investigation: IT, AA, GM, MV, AT; Visualization: IT; Supervision: AT, AA, MV; Writing—original draft: IT, AA, GM, MV, MO, AT; Writing—review & editing: IT, AA, GM, MV, MO, AT.

Acknowledgments

The expeditions were funded by the South African National Antarctic Programme through the National Research Foundation. AA and AT were funded by the ACE Foundation and Ferring Pharmaceuticals and the Australian Antarctic Science Program (project 4434). AA acknowledges support from the Japanese Society for the Promotion of Science (PE19055) and the London Mathematical Society (Scheme 5 – 52206). AT acknowledges support from the Australia Research Council (DP200102828). MV was supported by the NRF SANAP contract UID118745. GM acknowledges support from the Swedish Foundation for International Cooperation in Research and Higher Education (project no. SA2017-7063). IT and AT thank Dr J. Bidlot (ECMWF) and Dr L. Aouf (Meteo France) for support with the ERA5 products. We are indebted to Captain Knowledge Bengu and the crew of the SA Agulhas II for their invaluable contribution to data collection We acknowledge Dr L. Fascette for technical support.

References

Alberello, A., Bennetts, L., Heil, P., Eayrs, C., Vichi, M., MacHutchon, K., ... Toffoli, A. (2020). Drift of pancake ice floes in the winter antarctic marginal ice zone during polar cyclones. *Journal of Geophysical Research: Oceans*, *125*(3), e2019JC015418.

Alberello, A., Bennetts, L. G., Onorato, M., Vichi, M., MacHutchon, K., Eayrs, C., ... others (2022). Three-dimensional imaging of waves and floes in the marginal ice zone during a cyclone. *Nature communications*, *13*(1), 1–11.

Alberello, A., Onorato, M., Frascoli, F., & Toffoli, A. (2019). Observation of turbulence and intermittency in wave-induced oscillatory flows. *Wave Motion*, *84*, 81–89.

Andreas, E. L., Horst, T. W., Grachev, A. A., Persson, P. O. G., Fairall, C. W., Guest, P. S., & Jordan, R. E. (2010). Parametrizing turbulent exchange over summer sea ice and the marginal ice zone. *Quarterly Journal of the Royal Meteorological Society*, *136*(649), 927–943.

Audh, R. R., Johnson, S., Hambrock, M., Marquart, R., Pead, J., Rampai, T., ... Vichi, M. (2022, August). *Sea ice core temperature and salinity data collected during the 2019 SCALE Spring Cruise.* Zenodo. Retrieved from `https://doi.org/10.5281/zenodo.6997631` (This research has been funded by the National Research Foundation of South Africa (NRF)) doi: 10.5281/zenodo.6997631

Bechtold, P. (2009). Atmospheric thermodynamics. *ECMWF Lecture Notes*, *22*.

Bharti, V., Fairall, C. W., Blomquist, B. W., Huang, Y., Protat, A., Sullivan, P. P., ... Manton, M. J. (2019). Air-sea heat and momentum fluxes in the southern ocean. *Journal of Geophysical Research: Atmospheres*, *124*(23), 12426–12443.

Biri, S., Cornes, R. C., Berry, D. I., Kent, E. C., & Yelland, M. J. (2023). Airseafluxcode: Open-source software for calculating turbulent air-sea fluxes from meteorological parameters. *Frontiers in Marine Science*, *9*. doi: 10.3389/fmars.2022.1049168

Bourassa, M. A., Gille, S. T., Bitz, C., Carlson, D., Cerovecki, I., Clayson, C. A., ... Wick, G. A. (2013). High-latitude ocean and sea ice surface fluxes: Challenges for climate research. *Bulletin of the American Meteorological Society*, *94*(3), 403–423.

Brandt, R. E., Warren, S. G., Worby, A. P., & Grenfell, T. C. (2005). Surface albedo of the antarctic sea ice zone. *Journal of Climate*, *18*(17), 3606–3622.

Brouwer, J., Fraser, A. D., Murphy, D. J., Wongpan, P., Alberello, A., Kohout, A., ... Williams, G. D. (2022). Altimetric observation of wave attenuation through the antarctic marginal ice zone using icesat-2. *The Cryosphere*, *16*(6), 2325–2353. Retrieved from `https://tc.copernicus.org/articles/16/2325/2022/` doi: 10.5194/tc-16-2325-2022

Buck, A. L. (1981). New equations for computing vapor pressure and enhancement factor. *Journal of Applied Meteorology and Climatology*, *20*(12), 1527–1532.

Cerovečki, I., Sun, R., Bromwich, D. H., Zou, X., Mazloff, M. R., & Wang, S.-H. (2022). Impact of downward longwave radiative deficits on antarctic sea-ice extent predictability during the sea ice growth period. *Environmental Research Letters*, *17*(8), 084008.

Chin, T. M., Vazquez-Cuervo, J., & Armstrong, E. M. (2017). A multi-scale high-resolution analysis of global sea surface temperature. *Remote sensing of environment*, *200*, 154–169.

Dieckmann, G. S., & Hellmer, H. H. (2010). The importance of sea ice: an overview. *Sea ice*, *2*, 1–22.

Dong, S., Sprintall, J., Gille, S. T., & Talley, L. (2008). Southern ocean mixed-layer depth from argo float profiles. *Journal of Geophysical Research: Oceans*, *113*(C6).

ECMWF. (2016a). *IFS Documentation Cy41r2 Part IV: Physical Processes* (Tech. Rep.). European Centre for Medium-Range Weather Forecasts. Retrieved from `https://www.ecmwf.int/en/publications/ifs-documentation`

ECMWF. (2016b). *IFS Documentation Cy43r1 Part V: Ensemble Prediction System* (Tech. Rep.). European Centre for Medium-Range Weather Forecasts. Retrieved from `https://www.ecmwf.int/en/publications/ifs-documentation`

Fan, P., Pang, X., Zhao, X., Shokr, M., Lei, R., Qu, M., ... Ding, M. (2020). Sea ice surface temperature retrieval from landsat 8/tirs: Evaluation of five methods against in situ temperature records and modis ist in arctic region. *Remote Sensing of Environment*, *248*, 111975.

Fiddes, S. L., Protat, A., Mallet, M. D., Alexander, S. P., & Woodhouse, M. T. (2022). Southern ocean cloud and shortwave radiation biases in a nudged climate model simulation: does the model ever get it right? *Atmospheric Chemistry and Physics Discussions*, 1–34.

Flato, G., Marotzke, J., Abiodun, B., Braconnot, P., Chou, S. C., Collins, W., ... Rummukainen, M. (2014). Evaluation of climate models. In *Climate change 2013: the physical science basis. contribution of working group i to the fifth assessment report of the intergovernmental panel on climate change* (pp. 741–866). Cambridge University Press.

Gryschka, M., Drüe, C., Etling, D., & Raasch, S. (2008). On the influence of sea-ice inhomogeneities onto roll convection in cold-air outbreaks. *Geophysical Research Letters*, *35*(23).

Hall, D. K., Nghiem, S. V., Rigor, I. G., & Miller, J. A. (2015). Uncertainties of temperature measurements on snow-covered land and sea ice from in situ and modis data during bromex. *Journal of Applied Meteorology and Climatology*, *54*(5), 966–978.

Haumann, F. A., Moorman, R., Riser, S. C., Smedsrud, L. H., Maksym, T., Wong, A. P. S., ... Sarmiento, J. L. (2020). Supercooled southern ocean waters. *Geophysical Research Letters*, *47*(20), e2020GL090242.

Hepworth, E., Vichi, M., Engelbrecht, M., Kaplan, K., Sandru, A., Bossau, J., ... Rogerson, J. J. (2020). *Sea Ice Observations in the Antarctic Marginal Ice Zone during Spring 2019* [data set]. PANGAEA. Retrieved from `https://doi.org/10.1594/PANGAEA.921755` doi: 10.1594/PANGAEA.921755

Hersbach, H., Bell, B., Berrisford, P., Hirahara, S., Horányi, A., Muñoz-Sabater, J., ... others (2020). The era5 global reanalysis. *Quarterly Journal of the Royal Meteorological Society*, *146*(730), 1999–2049.

Horvat, C. (2021). Marginal ice zone fraction benchmarks sea ice and climate model skill. *Nature communications*, *12*(1), 1–8.

Horvat, C., & Tziperman, E. (2018). Understanding melting due to ocean eddy heat fluxes at the edge of sea-ice floes. *Geophysical Research Letters*, *45*(18), 9721–

9730.
Huguenin, M. F., Holmes, R. M., & England, M. H. (2022). Drivers and distribution of global ocean heat uptake over the last half century. *Nature Communications*, *13*(1), 1–11.
Johnson, J. H., Flittner, G. A., & Cline, M. W. (1965). *Automatic data processing program for marine synoptic radio weather reports* (No. 503). US Department of the Interior, Bureau of Commercial Fisheries.
Johnson, S., Audh, R. R., de Jager, W., Matlakala, B., Vichi, M., Womack, A., & Rampai, T. (2023). Physical and morphological properties of first-year antarctic sea ice in the spring marginal ice zone of the atlantic-indian sector. *Journal of Glaciology*, 1–14. doi: 10.1017/jog.2023.21
King, J. C., Marshall, G. J., Colwell, S., Arndt, S., Allen-Sader, C., & Phillips, T. (2022). The performance of the era-interim and era5 atmospheric reanalyses over weddell sea pack ice. *Journal of Geophysical Research*, *127*(9), e2022JC018805.
Kottmeier, C., & Engelbart, D. (1992). Generation and atmospheric heat exchange of coastal polynyas in the Weddell Sea. *Boundary-layer meteorology*, *60*(3), 207–234.
Krishfield, R. A., & Perovich, D. K. (2005). Spatial and temporal variability of oceanic heat flux to the arctic ice pack. *Journal of Geophysical Research: Oceans*, *110*(C7).
Kwok, R., Cunningham, G. F., & Hibler III, W. D. (2003). Sub-daily sea ice motion and deformation from radarsat observations. *Geophysical Research Letters*, *30*(23).
Landwehr, S., Volpi, M., Haumann, F. A., Robinson, C. M., Thurnherr, I., Ferracci, V., . . . Schmale, J. (2021). Exploring the coupled ocean and atmosphere system with a data science approach applied to observations from the antarctic circumnavigation expedition. *Earth System Dynamics*, *12*(4), 1295–1369. Retrieved from https://esd.copernicus.org/articles/12/1295/2021/ doi: 10.5194/esd-12-1295-2021
Li, N., Li, B., Lei, R., & Li, Q. (2020). Comparison of summer arctic sea ice surface temperatures from in situ and modis measurements. *Acta Oceanologica Sinica*, *39*(9), 18–24.
Liu, J., Xiao, T., & Chen, L. (2011). Intercomparisons of air–sea heat fluxes over the southern ocean. *Journal of climate*, *24*(4), 1198–1211.
Lytle, V., Massom, R., Bindoff, N., Worby, A., & Allison, I. (2000). Wintertime heat flux to the underside of east antarctic pack ice. *Journal of Geophysical Research: Oceans*, *105*(C12), 28759–28769.
Massom, R., & Comiso, J. C. (1994). The classification of arctic sea ice types and the determination of surface temperature using advanced very high resolution radiometer data. *Journal of Geophysical Research: Oceans*, *99*(C3), 5201–5218.
Massom, R. A., Lytle, V. I., Worby, A. P., & Allison, I. (1998). Winter snow cover variability on east antarctic sea ice. *Journal of Geophysical Research: Oceans*, *103*(C11), 24837–24855.
McCree, K. J. (1972). Test of current definitions of photosynthetically active radiation against leaf photosynthesis data. *Agricultural meteorology*, *10*, 443–453.
McPhee, M. G., Ackley, S. F., Guest, P., Huber, B. A., Martinson, D. G., Morison, J. H., . . . Stanton, T. P. (1996). The antarctic zone flux experiment. *Bulletin of the American Meteorological Society*, *77*(6), 1221–1232.
Merchant, C. J., Embury, O., Bulgin, C. E., Block, T., Corlett, G. K., Fiedler, E., . . . others (2019). Satellite-based time-series of sea-surface temperature since 1981 for climate applications. *Scientific data*, *6*(1), 1–18.
Millero, F. (1978). Freezing point of sea water. *eighth report of the Joint Panel of Oceanographic Tables and Standards, appendix*, *6*, 29–31.

Monin, A. S., & Obukhov, A. M. (1954). Basic laws of turbulent mixing in the surface layer of the atmosphere. *Contrib. Geophys. Inst. Acad. Sci. USSR*, *151*(163), e187.

Omatuku Ngongo, E., Audh, R. R., Hall, B., Skatulla, S., MacHutchon, K., Rampai, T., & Vichi, M. (2022, August). *Sea ice core temperature and salinity data collected during the 2019 SCALE Winter Cruise.* Zenodo. Retrieved from https://doi.org/10.5281/zenodo.6997449 (This research has been funded by the National Research Foundation of South Africa (NRF) Another version of this data set has been published in Skatulla, S., Audh, R.R., Cook, A., Hepworth, E., Johnson, S., Lupascu, D.C., MacHutchon, K., Marquart, R., Mielke, T., Omatuku, E. and Paul, F., 2022. Physical and mechanical properties of winter first-year ice in the Antarctic marginal ice zone along the Good Hope Line. The Cryosphere, 16(7), pp.2899-2925. - this data set was not quality controlled prior to publications. Future use of the data should refer to the dateset published here.) doi: 10.5281/zenodo.6997449

O'Carroll, A. G., Armstrong, E. M., Beggs, H. M., Bouali, M., Casey, K. S., Corlett, G. K., ... others (2019). Observational needs of sea surface temperature. *Frontiers in Marine Science*, *6*, 420.

Rasmussen, T. A., Høyer, J. L., Ghent, D., Bulgin, C. E., Dybkjær, G., Ribergaard, M. H., ... Madsen, K. S. (2018). Impact of assimilation of sea-ice surface temperatures on a coupled ocean and sea-ice model. *Journal of Geophysical Research: Oceans*, *123*(4), 2440–2460.

Ryan-Keogh, T., & Vichi, M. (2022, January). *Scale-win19 & scale-spr19 cruise report.* Zenodo. Retrieved from https://doi.org/10.5281/zenodo.5906324 doi: 10.5281/zenodo.5906324

Schmale, J., Baccarini, A., Thurnherr, I., Henning, S., Efraim, A., Regayre, L., ... Carslaw, K. S. (2019). Overview of the antarctic circumnavigation expedition: Study of preindustrial-like aerosols and their climate effects (ace-space). *Bulletin of the American Meteorological Society*, *100*(11), 2260-2283. doi: 10.1175/BAMS-D-18-0187.1

Skatulla, S., Audh, R. R., Cook, A., Hepworth, E., Johnson, S., Lupascu, D. C., ... Vichi, M. (2022). Physical and mechanical properties of winter first-year ice in the antarctic marginal ice zone along the good hope line. *The Cryosphere*, *16*(7), 2899–2925. doi: 10.5194/tc-16-2899-2022

Smith, S. D. (1988). Coefficients for sea surface wind stress, heat flux, and wind profiles as a function of wind speed and temperature. *Journal of Geophysical Research: Oceans*, *93*(C12), 15467–15472.

Talley, L. D. (2011). *Descriptive physical oceanography: an introduction.* Academic press.

Untersteiner, N. (1964). Calculations of temperature regime and heat budget of sea ice in the central arctic. *Journal of Geophysical Research*, *69*(22), 4755–4766.

Vichi, M. (2022). An indicator of sea ice variability for the antarctic marginal ice zone. *The Cryosphere*, *16*(10), 4087–4106.

Vichi, M., Eayrs, C., Alberello, A., Bekker, A., Bennetts, L., Holland, D., ... others (2019). Effects of an explosive polar cyclone crossing the antarctic marginal ice zone. *Geophysical Research Letters*, *46*(11), 5948–5958.

Womack, A., Vichi, M., Alberello, A., & Toffoli, A. (2022). Atmospheric drivers of a winter-to-spring lagrangian sea-ice drift in the eastern antarctic marginal ice zone. *Journal of Glaciology*, *68*(271), 999–1013. doi: 10.1017/jog.2022.14

Worby, A. P., & Comiso, J. C. (2004). Studies of the antarctic sea ice edge and ice extent from satellite and ship observations. *Remote sensing of environment*, *92*(1), 98–111.

Worby, A. P., Geiger, C. A., Paget, M. J., Van Woert, M. L., Ackley, S. F., & DeLiberty, T. L. (2008). Thickness distribution of antarctic sea ice. *Journal of Geophysical Research: Oceans*, *113*(C5).

Yu, L., Jin, X., & Schulz, E. W. (2019). Surface heat budget in the southern ocean from 42° s to the antarctic marginal ice zone: four atmospheric reanalyses versus icebreaker aurora australis measurements. *Polar Research*.

Yu, L., Jin, X., Schulz, E. W., & Josey, S. A. (2017). Air-sea interaction regimes in the sub-antarctic southern ocean and antarctic marginal ice zone revealed by icebreaker measurements. *Journal of Geophysical Research: Oceans*, *122*(8), 6547–6564.

Zwally, H. J., Comiso, J. C., Parkinson, C. L., Cavalieri, D. J., & Gloersen, P. (2002). Variability of antarctic sea ice 1979–1998. *Journal of Geophysical Research: Oceans*, *107*(C5), 9–1.

Figure 1.

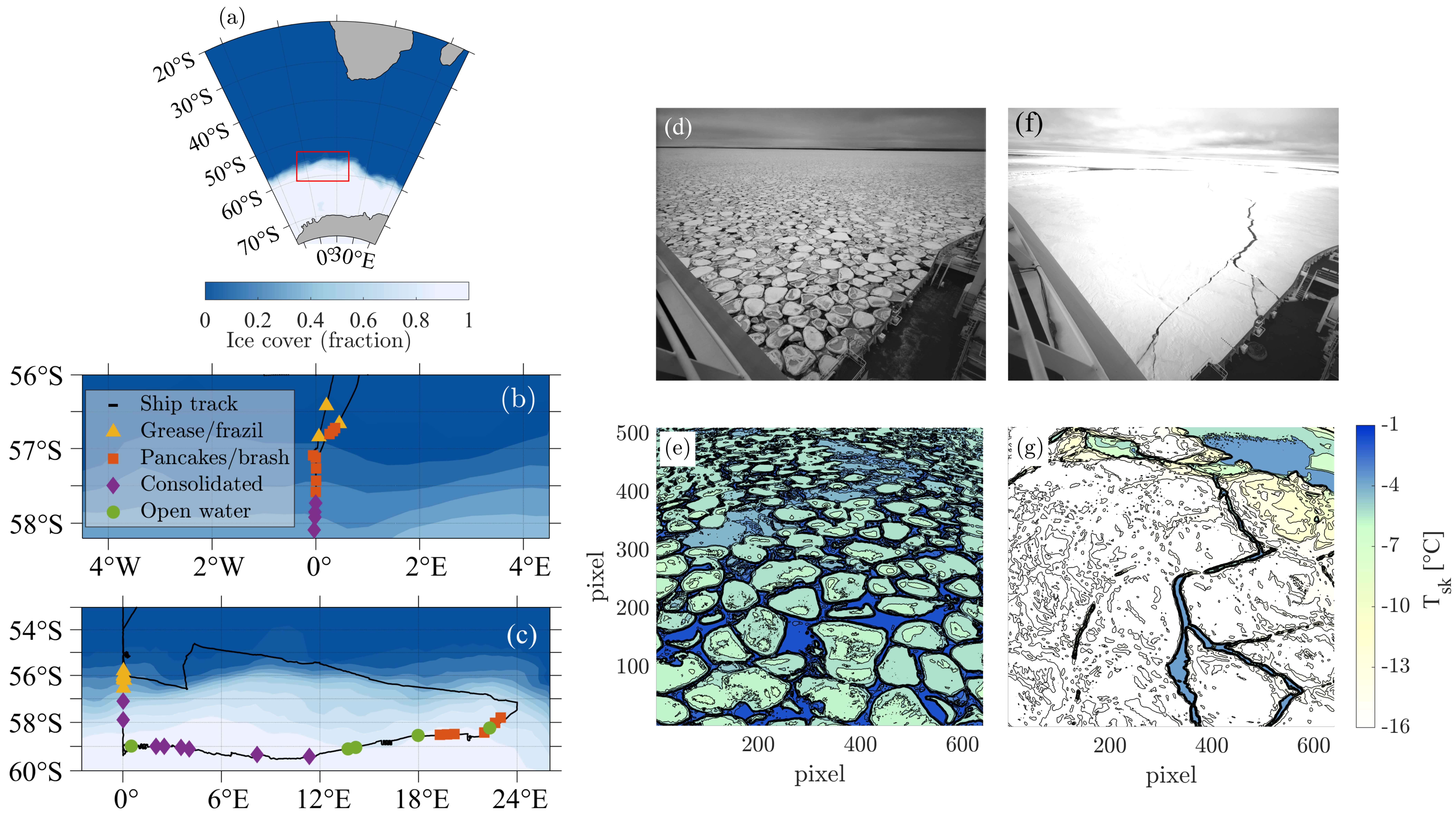

(a)
20°S
30°S
40°S
50°S
60°S
70°S
0°
30°E
0
0.2
0.4
0.6
0.8
1
Ice cover (fraction)
(b)
Ship track
Grease/frazil
Pancakes/brash
Consolidated
Open water
56°S
57°S
58°S
4°W
2°W
0°
2°E
4°E
(c)
54°S
56°S
58°S
60°S
0°
6°E
12°E
18°E
24°E
(d)
(f)
(e)
(g)
500
400
300
200
100
pixel
200
400
600
pixel
T_{sk} [°C]
-1
-4
-7
-10
-13
-16

Figure 2.

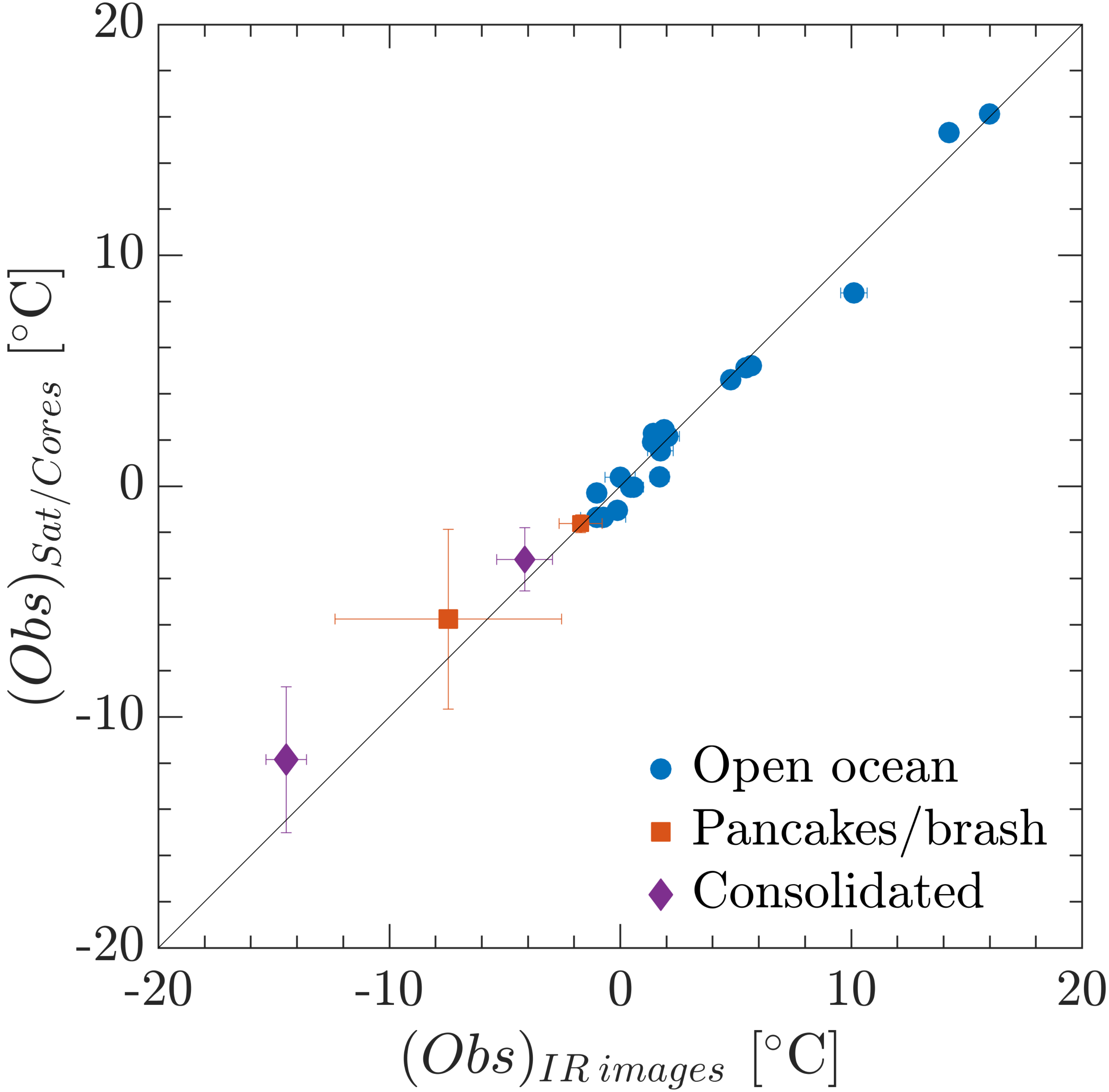

20
10
0
-10
-20
-20
-10
0
10
20
$(Obs)_{Sat/Cores}$ [°C]
$(Obs)_{IR\ images}$ [°C]
Open ocean
Pancakes/brash
Consolidated

Figure 3.

(a)
Grease/frazil
Pancakes/brash
Consolidated
T_A
C_i
T_f
T_{sk} [°C]
C_i [%]
Distance from ice edge [km]
45 70 95 120 145 170 195 220
26/07, 12:00
27/07, 00:00
27/07, 12:00
28/07, 00:00
28/07, 12:00
(b)
45 km from edge
$C_i = 40\%$
Grease/frazil
(c)
110 km from edge
$C_i = 90\%$
Pancakes
(d)
130 km from edge
$C_i = 100\%$
Pancakes
(e)
220 km from edge
$C_i = 100\%$
Consolidated
pdf
T_{sk} [°C]

Figure 4.

Grease/frazil
Pancakes/brash
Consolidated
Open water
T_A
C_i
T_f
T_{sk} [$\circ C$]
C_i [%]
(a)
22/10
24/10
26/10
28/10
30/10
01/11
03/11
Distance fro ice edge [km]
30
110
190
270
350
430
pdf
(b)
60 km from edge
C_i = 10%
Grease/frazil
(c)
250 km from edge
C_i = 50%
Pancake/brash
(d)
340 km from edge
C_i = 0%
Open water
(e)
430 km from edge
C_i = 100%
Consolidated
T_{sk} [°C]

Figure 5.

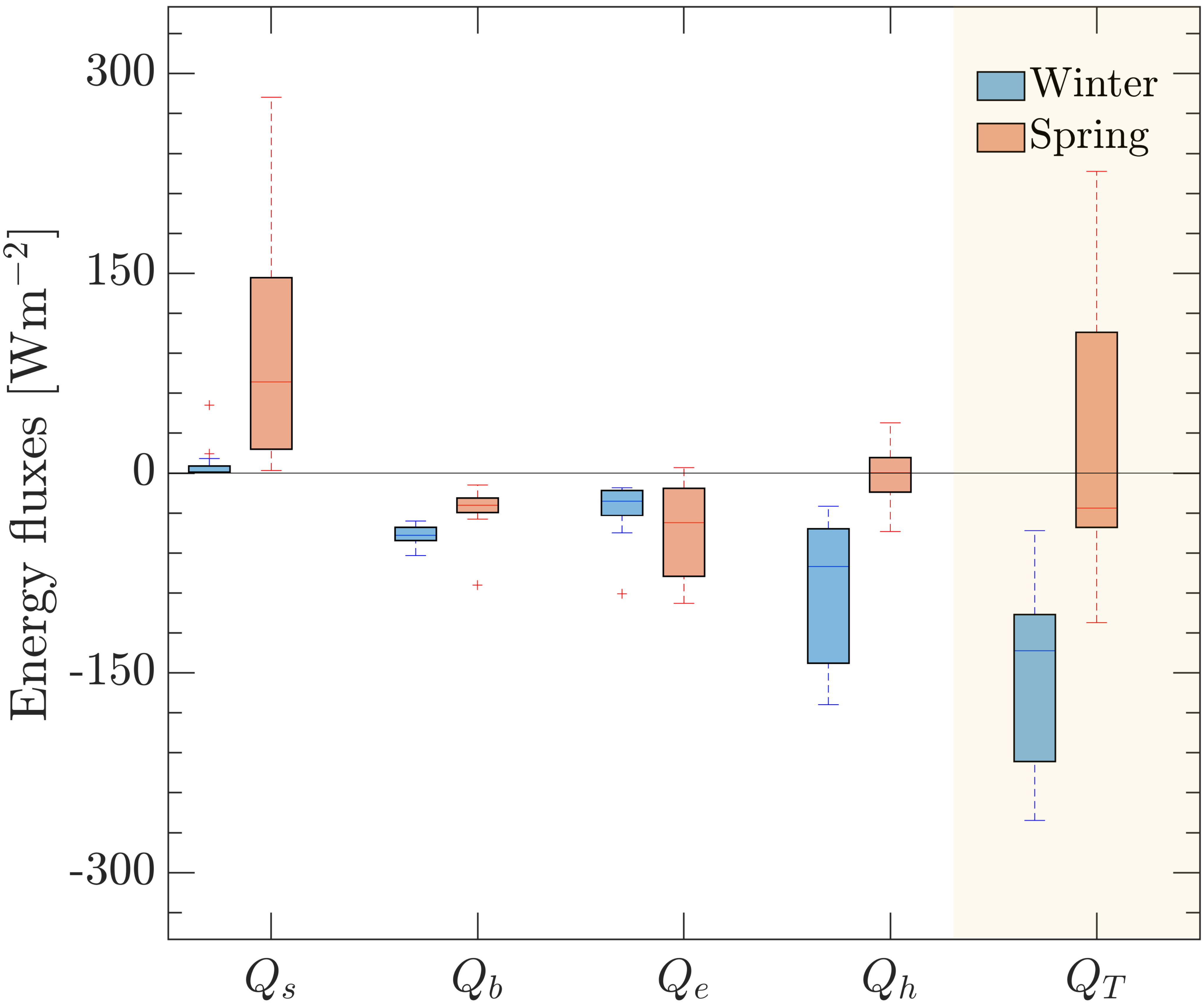

Energy fluxes [Wm^{-2}]
300
150
0
-150
-300
Q_s
Q_b
Q_e
Q_h
Q_T
Winter
Spring

Figure 6.

Grease/frazil
Pancakes/Brash
Consolidated
Open water
RMSE: 35%
(a)
$(C_i)_{ERA5}$ [%]
$(C_i)_{Obs}$ [%]
RMSE: 39%
(b)
0
20
40
60
80
100

Figure 7.

(a)
RMSE: 5.2 °C
(b)
RMSE: 1.0 °C
(c)
RMSE: 1.7 °C
(d)
RMSE: 1.4 °C
$(SST \ \& \ ISTL1)_{ERA5}$ [°C]
$(T_{sk})_{ERA5}$ [°C]
$(T_{sk})_{Obs}$ [°C]
Open ocean
Grease/frazil
Pancakes/Brash
Consolidated
Open water
Cores

Figure 8.

(a)
RMSE:
34.8 Wm^{-2}
$(Q_s)_{ERA5}$ [W m^{-2}]
$(Q_s)_{Obs}$ [W m^{-2}]
(b)
RMSE:
9.8 Wm^{-2}
$(Q_b)_{ERA5}$ [W m^{-2}]
$(Q_b)_{Obs}$ [W m^{-2}]
(c)
RMSE:
15.8 Wm^{-2}
$(Q_e)_{ERA5}$ [W m^{-2}]
$(Q_e)_{Obs}$ [W m^{-2}]
(d)
RMSE:
32.5 Wm^{-2}
$(Q_h)_{ERA5}$ [W m^{-2}]
$(Q_h)_{Obs}$ [W m^{-2}]
(e)
RMSE:
62.5 Wm^{-2}
$(Q_T)_{ERA5}$ [W m^{-2}]
$(Q_T)_{Obs}$ [W m^{-2}]
(f)
RMSE:
36.6 Wm^{-2}
$(Q_T)_{ERA5}^{(T_{sk})^{Obs}}$ [$W m^{-2}$]
$(Q_T)_{Obs}$ [W m^{-2}]
Grease/frazil
Pancakes/Brash
Consolidated

Figure 9.

(a)
RMSE: 81.2 Wm^{-2}
$(Q_s)_{ERA5}$ [W m^{-2}]
$(Q_s)_{Obs}$ [W m^{-2}]
(b)
RMSE: 7.2 Wm^{-2}
$(Q_b)_{ERA5}$ [W m^{-2}]
$(Q_b)_{Obs}$ [W m^{-2}]
(e)
RMSE: 108.7 Wm^{-2}
$(Q_T)_{ERA5}$ [W m^{-2}]
$(Q_T)_{Obs}$ [W m^{-2}]
Grease/frazil
Pancakes/Brash
Consolidated
Open water
(c)
RMSE: 44.9 Wm^{-2}
$(Q_e)_{ERA5}$ [W m^{-2}]
$(Q_e)_{Obs}$ [W m^{-2}]
(d)
RMSE: 33.9 Wm^{-2}
$(Q_h)_{ERA5}$ [W m^{-2}]
$(Q_h)_{Obs}$ [W m^{-2}]
(f)
RMSE: 57.7 Wm^{-2}
$(Q_T)_{ERA5}^{(Q_s)Obs}$ [W m^{-2}]
$(Q_T)_{Obs}$ [W m^{-2}]

Figure A1.


(a)
RMSE:
20.9 Wm^{-2}
$(Q_b)^{direct}_{ERA5}$ [Wm^{-2}]
$(Q_b)^{from\ variables}_{ERA5}$ [Wm^{-2}]
(b)
RMSE:
24.1 Wm^{-2}
$(Q_e)^{direct}_{ERA5}$ [Wm^{-2}]
$(Q_e)^{from\ variables}_{ERA5}$ [Wm^{-2}]
(c)
RMSE:
10.8 Wm^{-2}
$(Q_h)^{direct}_{ERA5}$ [Wm^{-2}]
$(Q_h)^{from\ variables}_{ERA5}$ [Wm^{-2}]
50
0
-50
-100
-150
-200
-250
-200
-100
0

Figure B1.

Open ocean
Grease/frazil
Pancakes/brash
Consolidated
Open water
(a)
(b)
(c)
(d)
(e)
(f)
(g)
(h)
RMSE: 32.4 Wm^{-2}
RMSE: 1.3 °C
RMSE: 2.4 ms^{-1}
RMSE: 0.8 gkg^{-1}
RMSE: 141.7 Wm^{-2}
RMSE: 2.0 °C
RMSE: 3.0 ms^{-1}
RMSE: 0.6 gkg^{-1}
$(Q_{s_d})_{ERA5}$ [Wm^{-2}]
$(T_A)_{ERA5}$ [°C]
$(u)_{ERA5}$ [ms^{-1}]
$(q_s - q_a)_{ERA5}$ [g kg^{-1}]
$(Q_s)_{Obs}$ [Wm^{-2}]
$(T_A)_{Obs}$ [°C]
$(u)_{Obs}$ [ms^{-1}]
$(q_s - q_a)_{Obs}$ [g kg^{-1}]